PROCEEDINGS, 51st Workshop on Geothermal Reservoir Engineering
Stanford University, Stanford, California, February 9-11, 2026
SGP-TR-230

Rapid Dynamic Reservoir Modeling and Sensitivity Analysis of the Utah FORGE Project using Fast Marching Method-based Simulation

Chin-Hsiang Chan and Akhil Datta-Gupta

Texas A&M University, College Station, TX, USA

keisyo@tamu.edu

Keywords: enhanced geothermal system, reduced order model, sensitivity studies, reservoir modeling, geomechanics

ABSTRACT

Simulating long-term performance of enhanced geothermal systems (EGS) is computationally intensive, limiting the scope of reservoir model calibration and sensitivity analysis. This work introduces a novel reduced-order model, Fast Marching Method-based Simulation (FMM-SIM) to accelerate the geothermal reservoir simulation to make it feasible for field applications and demonstrates its applicability using the Utah FORGE project. The proposed FMM-SIM is a reduced-order modeling approach that transforms 3D fine-scale simulation into a multi-resolution representation using Diffusive Time of Flight (DTOF) which represents the propagation time of the 'pressure front' in the reservoir. Our method utilizes a finite-volume Fast Marching Method to efficiently compute DTOF, which then serves as the spatial coordinate for the multi-resolution representation. To ensure accuracy, full 3D resolution is retained near the wellbore and hydraulic fractures, while the remainder of the reservoir is represented by a sequence of 1D grid. The 3D and 1D domains are connected through non-neighbor connections that account for both fluid and heat transmissibility. Whereas conventional reservoir simulations can be computationally intensive to capture complex physics including thermal, compositional and geomechanical effects, FMM-SIM preserves the essential details while reducing high-fidelity simulation time by orders of magnitude.

We applied the proposed method to a synthetic model and the Utah FORGE model, achieving around 15x speedup in simulation time, allowing field-scale simulation to finish in about one hour. Using a synthetic model designed after a commercial-scale EGS project, we examined the influence of key parameters in EGS development, including connectivity, conductivity and conformance as well as, geomechanical effects and well control on thermal breakthrough. Barton-Bandis fracture closure model represents fracture closure and dilation during fluid circulation. We also evaluated intermittent thermal extraction strategies that aim to postpone premature thermal breakthrough. Subsequently, we carried out data assimilation using a multi-objective genetic algorithm to construct a dynamic reservoir model for the Utah FORGE project that integrates diverse datasets such as the discrete fracture network (DFN) model, native-state model, distributed strain sensing (DSS) measurements, and one month of circulation test data. Integrating the geomechanical module enhanced the quality of the history match and indicated that some degree of fracture closure occurred during the circulation period. The calibrated model was then used to test intermittent thermal extraction strategies at the Utah FORGE site, revealing the balance between energy production rate and long term cumulative energy recovery when the production well is periodically shut in. All simulation studies are grounded by accelerated reservoir simulations using FMM-SIM, which enables comprehensive parametric studies and dynamic reservoir modeling. The results demonstrate that FMM-SIM is an effective tool for optimizing geothermal energy extraction through fast and reliable reservoir simulation.

1. INTRODUCTION

Enhanced geothermal system (EGS) is designed to extract thermal energy from subsurface formations with limited natural water availability. In an EGS, fluid is injected into the reservoir and circulated through a stimulated zone that establishes hydraulic connectivity between the injection and the production wells. As the fluid migrates through the hot rock matrix, it absorbs thermal energy and is subsequently produced at elevated temperatures. This circulation process enables efficient heat extraction from geothermal resources that are otherwise difficult to exploit using conventional methods. Interest in EGS has grown rapidly over the past decade as part of the broader shift toward renewable energy (Horne et al., 2025). Within the United States, EGS development follows two distinct paths involving public research and private commercialization. The Utah Frontier Observatory for Research in Geothermal Energy (FORGE) (Moore & McLennan, 2018), which receives support from the United States Department of Energy, serves as the premier site for testing EGS methodologies within a controlled environment. In parallel, commercial scale deployment has achieved significant milestones. Fervo Energy successfully commissioned a pioneering EGS facility in northern Nevada (Norbeck & Latimer, 2023) and announced plans for a massive expansion near the Utah FORGE site that targets a several hundred megawatt scale trajectory (Norbeck et al., 2024). The integration of geothermal power into the portfolios of major technology companies like Google, which now utilizes electricity from Fervo Energy for its data centers, illustrates a rising market demand fueled by the energy intensive nature of artificial intelligence and data center expansion (Terrell, 2021). This rapid scaling increases the stakes for project longevity. These milestones highlight the urgent need to characterize long-term EGS reservoir behavior and thermal drawdown in order to ensure the technical and economic sustainability of future large scale deployments.

One of challenges which most EGS project faces are premature thermal breakthroughs. During the injection of cool fluid from the injector, cold thermal front propagates to the producer. When the cold thermal front reaches the producer, there is significant decline of thermal output, which often makes the project economically unviable. EGS project especially suffers from this premature thermal breakthrough as injected fluid flows through the stimulated zone. Several approaches are suggested to mitigate the premature thermal breakthrough in EGS (Liu et al., 2025). (i) Managing injection and production rates can prevent premature cooling of the production wells (Dehdouh et al., 2024). This strategy is particularly effective in multi-well applications, allowing flow rates to be reallocated to delay thermal breakthrough. (ii) Effective stimulation in EGS reservoir can avoid channelized preferential flow paths and maximize the heat exchange area, thereby, enhance the thermal recovery. (iii) Intermittent thermal extraction, which alternates periods of active heat extraction with shut-in or resting phases, allows reservoir to recover thermally. (iv) Circulating CO_2 instead of water could improve the sweep of the rock matrix and fosters a more comprehensive heat exchange within fracture networks (Cong et al., 2024). (v) Managing fracture conductivity with temperature-sensitive proppants helps regulate fluid flow within fractures (Al Balushi et al., 2023). For instance, by increasing flow resistance in cooler, depleted zones and maintaining higher conductivity in hotter, unexploited regions, this approach prolongs the contact time between the circulating fluid and the hot rock. Among the various strategies to prevent premature thermal breakthrough, flow management in EGS wells is the most practical and readily implemented option. Other methods, such as stimulation design and the use of temperature-sensitive proppants, must be planned before well completion, and approaches like CO_2-based circulation require additional preparation and cost. Therefore, this work focuses on well control of EGS operations, especially for intermittent thermal extraction strategies.

Geomechanical effects represent another critical consideration for the viability of EGS. Horne et al. (2025) noted that several EGS developments face operational constraints stemming from induced seismicity. EGS projects require high volume fluid circulation to maximize thermal extraction from the reservoir. While mass balance could be maintained through fluid extraction, localized pore pressure elevation occurs rapidly near injection wells. Such pressure increases can destabilize preexisting faults and trigger seismic events. Furthermore, EGS operations involve complex fracture stimulation between injection and production wells. As circulation proceeds, thermal and mechanical stressors may cause fracture closure near production zones which increase hydraulic resistance. These geomechanical shifts alter the fundamental relationship between flow rates and bottom hole pressure behavior, thereby complicating the accuracy of subsurface reservoir modeling.

Simulating well thermal performance in EGS is crucial for project development and management. To estimate the thermal performance of EGS wells, numerical simulations provide high-fidelity solutions as they solve mass and energy conservation equations in subsurface systems. However, this numerical simulation in EGS tends to be computationally intensive, as the process of thermal recovery in EGS involves strongly coupled and highly nonlinear processes, including thermal, compositional, and geomechanical effects with complex matrix-fracture interaction. In addition, large simulation domains are required to capture continuous heat replenishment from the surrounding formation. These factors collectively lead to severe numerical convergence challenges and high computational cost. For large field scale models, such as the Utah FORGE site, EGS reservoir simulations typically require several hours to days to complete.

To address these challenges, this work introduces a novel reduced order modeling framework, the Fast Marching Method-based Simulation (FMM-SIM), designed to accelerate EGS reservoir simulations and enable practical field applications, including the Utah FORGE project. The proposed FMM-SIM transforms 3D fine-scale simulation into a multi-resolution representation using Diffusive Time of Flight (DTOF) which represents the propagation time of the ‘pressure front’ in the reservoir. Our proposed method utilizes a finite-volume FMM to efficiently compute DTOF, which then serves as the spatial coordinate for the multi-resolution representation. To ensure accuracy, full 3D resolution is retained near the wellbore and hydraulic fractures, while the remainder of the reservoir is represented by a sequence of 1D grid. The 3D and 1D domains are connected through non-neighbor connections that account for both fluid and heat transmissibility. By retaining essential physics while significantly reducing spatial complexity, FMM-SIM achieves orders of magnitude reduction in computational time compared with conventional high-fidelity EGS simulations while incorporating thermal, compositional, and geomechanical processes.

This paper is structured as follows. *Introduction* section gives general background of EGS projects. The *methodology* section introduces the reduced order model and flow-geomechanical coupling during simulation. *Application* section first conducts sensitivity analysis including 3 major factors in fluid flow (connectivity, conductivity and conformance), geomechanical effects and well control on thermal breakthrough using a synthetic model designed after one of the commercial-scale EGS projects. Subsequently, the proposed reduced order simulation framework is applied to the Utah FORGE project to perform data assimilation for the construction of a dynamic reservoir model and to optimize well control strategies through intermittent thermal extraction.

2. METHODOLOGY

2.1 Fast Marching Method-based Rapid Reservoir Simulation (FMM-SIM)

A novel reduced order modeling method has been developed that transforms the 3D physical domain into a multi-resolution domain consisting of a preserved 3D domain and an upscaled 1D domain along the DTOF contours. The applicability of FMM-SIM in EGS reservoir has been demonstrated for both water-based EGS (Chan et al., 2026) and CO2-based EGS (Chan, Onishi, et al., 2025). Our proposed rapid reservoir simulation method is based on the finite-volume-based formulation of FMM proposed by Chen et al. (2023). This approach enables the construction of a multi-resolution reservoir model in which DTOF serves as the spatial coordinate, allowing efficient simulation while preserving fine-scale resolution near the wellbore and hydraulic fractures.

2.1.1 Diffusive Time of Flight (DTOF) and Fast Marching Method (FMM)

DTOF represents the contours of peak arrival time of pressure front propagation corresponding to an impulse source (Datta-Gupta et al., 2011). This variable is based on analogy between pressure propagation and wave propagation. The DTOF is derived from the diffusivity equation for fluid flow in heterogeneous permeable media, shown in Eq. 1.

$$\phi(x)\mu c_t \frac{\partial P(x,t)}{\partial t} = \nabla \cdot \left[\vec{k}(x)\nabla P(x,t)\right] \tag{1}$$

where x is the spatial variable, t is time, ϕ is reservoir porosity, μ is fluid viscosity, c_t is total compressibility, P is pressure, k is reservoir permeability. An asymptotic approach from the asymptotic ray theory is utilized to solve the Fourier transformed form of Eq. 1. This method has proven effective for analyzing front propagation in general (Sethian, 1996). Based on previous work in diffusive electromagnetic imaging and hydrology (Datta-Gupta et al., 2001; Vasco et al., 2000; Virieux et al., 1994), the asymptotic pressure solution is expressed as an infinite series as below.

$$\tilde{P}(x,\omega) = \exp\left[-\sqrt{-i\omega}\,\tau(x)\right]\sum_{k=0}^{\infty}\frac{A_k(x)}{\left(\sqrt{-i\omega}\right)^k} \tag{2}$$

where ω represents frequency, $\tau(x)$ represents the phase of a propagating wave and thus, describes the geometry of the propagation front. We denote this variable τ as DTOF, the diffusive time of flight. $A_k(x)$ are real functions that relate to the amplitude of the wave involving summation of infinite term. Essential physical quantities are captured within just the first few terms, providing a concise yet accurate representation of the system's behavior. Focusing on the leading-order term ($k = 0$) provides the following equation as high frequency asymptotic solution of the diffusivity equation (Datta-Gupta & King, 2007).

$$\nabla^T\tau(x)\cdot\vec{k}(x)\cdot\nabla\tau(x) = \phi(x)\mu c_t \tag{3}$$

where $\vec{k}$ represents the permeability tensor. Eq. 3 represents a form of the well-known Eikonal equation, commonly used to represent wave propagation behaviors. This Eikonal equation has been extended for multi-phase flow by replacing the fluid viscosity to mobility.

$$\nabla^T\tau(x)\cdot\vec{k}(x)\cdot\nabla\tau(x) = \frac{\phi(x)c_t}{\sum_p M_p(x)},\quad M_p(x) = \frac{k_{r,p}(x)}{\mu_p(x)} \tag{4}$$

where M_p is fluid mobility, k_r is relative permeability and subscript p indicates fluid phases. Chen et al. (2021) extended Eq. 4 with finite-volume-based formulation for computing DTOF in general grid geometries. Integrating within a finite representative volume and using the divergence theorem provide the following formulation of the Eikonal equation that utilizes the pore volume and transmissibility.

$$\sum_{m(n)}^{\tau_m<\tau_n} T_{nm}\cdot(\tau_n-\tau_m)^2 = \frac{c_t V_{p,n}}{M_n} \tag{5}$$

where T_{nm} is transmissibility between cell n and m, τ_n is DTOF at cell n, $V_{p,n}$ is pore volume of cell n, and M_n is the fluid mobility in cell n. The notation of $\tau_m < \tau_n$ indicates only upstream cells are considered and $m(n)$ indicates connections of cell n. In other words, only upstream connections are considered in Eq. 5. Since the DTOF value of a grid block depends solely on that of the upstream blocks, the solution can be systematically constructed from lower to higher DTOF values. Such strategy is developed as a numerical algorithm called the Fast Marching Method (FMM) by Sethian (1999). Though original work of FMM was designed in finite difference scheme, Chen et al. (2021) extended this approach to a finite volume scheme. Figure 1 illustrates the computation of DTOF using FMM on finite volume grids. The finite volume FMM calculates DTOF through the following steps:

(a) DTOF propagation begins from the well completion cells where the DTOF values are assigned as zero.
(b) DTOF values in neighboring cells are computed using Eq. 5.
(c) The neighboring cell with the minimum DTOF value is identified and marked as accepted.
(d) DTOF values in the neighbors of the newly accepted cell are then computed and the cell with minimum DTOF value is updated. This process is repeated until all cells are accepted.

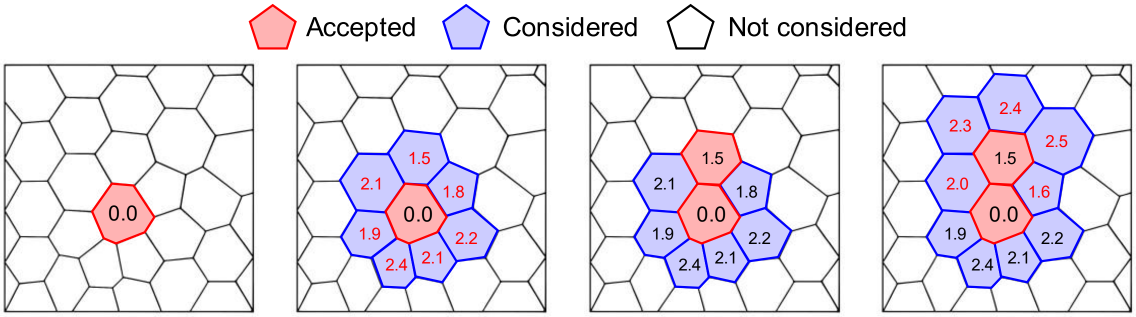

(a) (b) (c) (d)

Figure 1: Illustration of the FMM in finite volume grids. The numbers inside the grid cells represent DTOF values. Red numbers indicate newly calculated or updated DTOF values, while black numbers represent previously computed values. Figure from Chan, Kumawat, et al. (2025).

2.1.2 Fast Marching Method-based Multi-resolution Modeling

Figure 2 describes the general workflow of FMM-based multi-domain, multi-resolution reservoir modeling. This approach converts the full 3D model to an equivalent multi-resolution model using DTOF as the spatial coordinate. Beginning with a full 3D reservoir model, DTOF is first calculated using the FMM. Based on the contours of DTOF, cells are grouped to define multiple DTOF levels where the volume enclosed by two DTOF contours constitute one level. For multi-well applications, the model is divided into local domains, representing individual well drainage areas, and a shared domain that captures interference among wells.

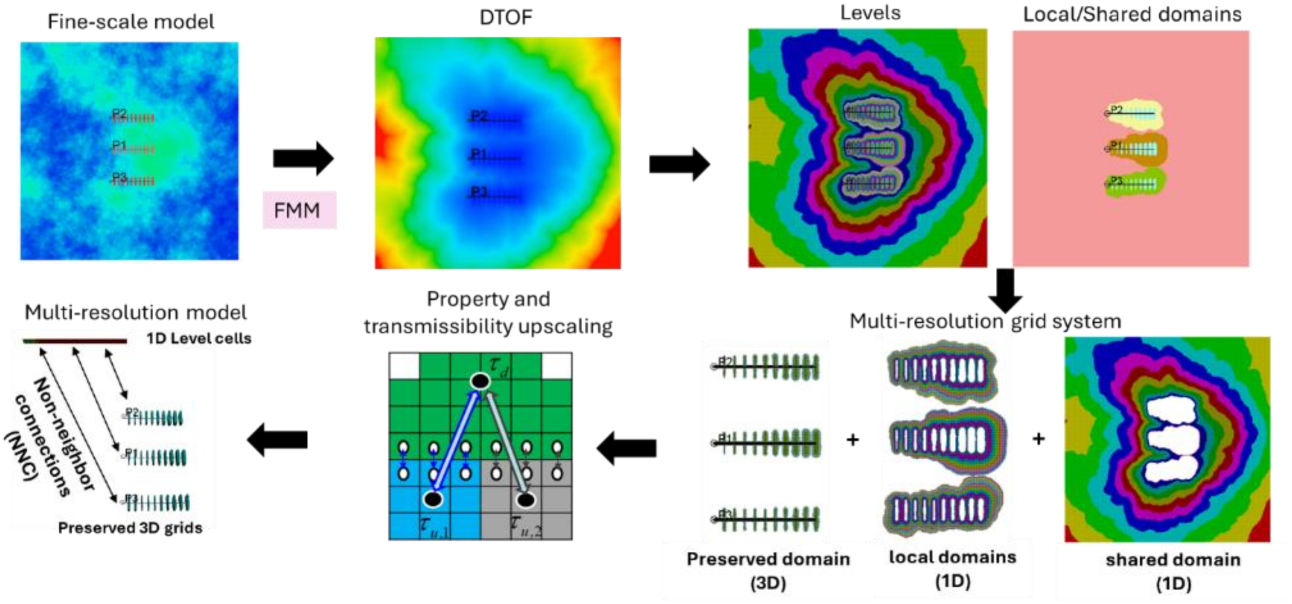

Figure 2: Fast marching-based multi-domain, multi-resolution simulation workflow (Chan, Datta-Gupta, & Shor, 2025; Chen et al., 2023).

Chan et al. (2026) showed that DTOF has a strong positive linear relationship with reservoir pressure and temperature. Therefore, we convert the DTOF levels into a sequence of 1D grids. Typically, the near-wellbore region is maintained at the original 3D resolution to capture complex flow patterns, such as flow through fractures to matrix, gravity effects, and mobility changes. Hence, the resulting model has a multi-resolution grid system, 3D grids near the wellbore and 1D grids for the rest of the grid system. The preserved 3D grids and 1D grids are connected through non-neighbor connections (NNCs) with the outermost cells in the preserved domain and the first cell in the 1D domain. After the multi-resolution grid is defined, the properties and transmissibilities of the upscaled model are computed. Most properties are obtained by pore volume weighting of fine-scale grid values within individual DTOF levels, and transmissibilities are computed using following equations (Chan et al., 2026; Chen et al., 2021).

$$\mathrm{T_{nm}} = \frac{\mathrm{\mu c_t V_{p,n}}}{(\mathrm{\tau_n} - \mathrm{\tau_m})^2} \tag{6}$$

$$\mathrm{H_{i\to j}} = \bar{\alpha}_{\mathrm{ij}} \cdot \mathrm{T_{i\to j}}, \quad \bar{\alpha}_{\mathrm{ij}} = \frac{\mathrm{\alpha_i} + \mathrm{\alpha_j}}{2}, \quad \mathrm{\alpha_i} = \frac{\mathrm{\kappa_i}}{\mathrm{k_i}} \tag{7}$$

Multi-resolution modeling in geothermal application requires to define two distinct transmissibilities: one for fluid flow and another for heat transfer. Fluid transmissibility T is derived from the finite volume formulation of the Eikonal equation, yielding an expression based on DTOF that enables consistent upscaling of flow behavior. While advective heat transport can be directly represented using this fluid transmissibility, conductive heat transfer through the solid matrix requires a separate treatment. To address this, thermal transmissibility H is computed using a proportional relationship between fluid and thermal transmissibility as shown in Eq. 7, defined through a thermal conversion factor α that depends on the ratio of thermal conductivity κ to permeability k. The resulting intercell heat transmissibility is obtained by applying an average thermal conversion factor to the corresponding fluid transmissibility, allowing both advective and conductive heat transfer processes to be efficiently represented within the multi resolution framework.

2.2 Barton-Bandis Fracture Closure Model

To represent fracture closure behavior during production, the Barton-Bandis fracture closure model is adopted in this study. The Barton-Bandis model is an empirical formulation that describes fracture closure induced by pressure depletion, capturing the associated reduction in fracture permeability as fracture close under increasing effective normal stress. This joint-closure model, developed from an extensive body of experimental data, was introduced by Barton et al. (1985) and is expressed as,

$$\mathrm{\sigma_n'} = \frac{\mathrm{\Delta V_j} K_n}{1 - \mathrm{\Delta V_j}/V_m} \tag{8}$$

where σ_n' is the effective normal stress, and ΔV_j is the fracture closure under effective normal stress, and K_n is the normal fracture stiffness, and V_m is the maximum possible fracture closure.

By rearranging Eq. 8, Park et al. (2019) defined the transmissibility multiplier as follows

$$\mathrm{T_{mult}} = \left[1 - \frac{\Delta \mathrm{P}\left(1 - \mathrm{k_{rf}^{0.25}}\right)}{\mathrm{K_n w_{init}}\left(1 - \mathrm{k_{rf}^{0.25}}\right) + \Delta \mathrm{P}}\right]^4 \tag{9}$$

where ΔP is pressure depletion, w_{init} is the initial fracture width, k_{rf} is the fracture residual permeability ratio, which is defined as a ratio of residual permeability to initial permeability. The value of k_{rf} depends on fracture surface roughness, fracture-matrix mechanical properties, and the presence or absence of proppants within the fracture.

The pore-volume multiplier is derived using an empirical permeability-porosity relationship. This concept was first introduced by Davies and Davies (2001) based on experimental observations and was later refined by several studies to enhance its applicability in numerical simulations (Rutqvist & Tsang, 2002; Wu et al., 2014). In this formulation, the pore volume multiplier is assumed to follow a log linear relationship with the transmissibility multiplier. The porosity-permeability coefficient, c_{pp}, appears as the proportionality constant associated with the logarithm of transmissibility multiplier, as expressed in Eq. 10. The value of c_{pp} is rock-dependent, reflecting variations in mechanical and hydraulic responses among different lithologies (Davies & Davies, 2001).

$$\mathrm{PV_{mult}} = \frac{1}{\mathrm{c_{pp}}} \cdot \ln(\mathrm{T_{mult}}) + 1 \tag{10}$$

3. COMMERCIAL-SCALE SYNTHETIC MODEL

3.1 Synthetic EGS Modeling and FMM Application

A synthetic reservoir model is developed based on a real field EGS project in northern Nevada. This project represents a first of its kind commercial-scale EGS development located adjacent to the Blue Mountain geothermal field and is hydraulically connected to an existing power generation facility (Norbeck et al., 2024). This site features a doublet horizontal well consisting of an injector (34A-22) and a producer (34-22) where both wells are hydraulically stimulated to create flow path between wells. The reservoir domain is defined based on reported microseismic clouds, resulting in 110×350×10 grids (385,000 cells in total). Details about modeling this synthetic model are described in Appendix A. Using this model, cool water is injected with temperature value at bottomhole of 105 °F, and producer is controlled by BHP value of 3000 psi. The simulation is run for 50 years to evaluate life-scale geothermal performances.

Figure 3 shows the results of reservoir simulation in the synthetic model. The production fluid temperature is relatively stable for the initial 2 years and starts declining as cold thermal front reaches the producer. According to the techno-economic analysis conducted by NREL (Augustine et al., 2023), the abandonment temperature is defined as 300 °F (150 ℃). With continuous injections, this reservoir reached the abandonment temperature after 14 years of operations, and until then 5040 GWh of thermal energy was produced. Figure 3(b) shows the injection and production rates, where injection rate is constant at 63 L/s and production rate has slightly smaller value due to the fluid losses, while more than 98 % of injected fluid is recovered from producer. Figure 3(c) and (d) shows the reservoir temperature and pressure after 50 years of operations. We can observe thermal front propagation from the injector and pressure reduction in the reservoir. Observations indicate that the cold front propagates more extensively within the lower layer. This phenomenon is attributable to several factors. First, gravitational effects are significant, as the cooler, denser injected fluid naturally sinks. Second, this is potentially amplified by the geothermal gradient; the higher ambient temperatures in the lower layer create a larger temperature differential relative to the cold injectate, which enhances the conductive heat transfer. Finally, the propagation path in upper layer may be constrained by production dynamics, as the location of the producer's outlet might limit fluid propagating in upper layer, thus limiting the cool front's migration in upper layers.

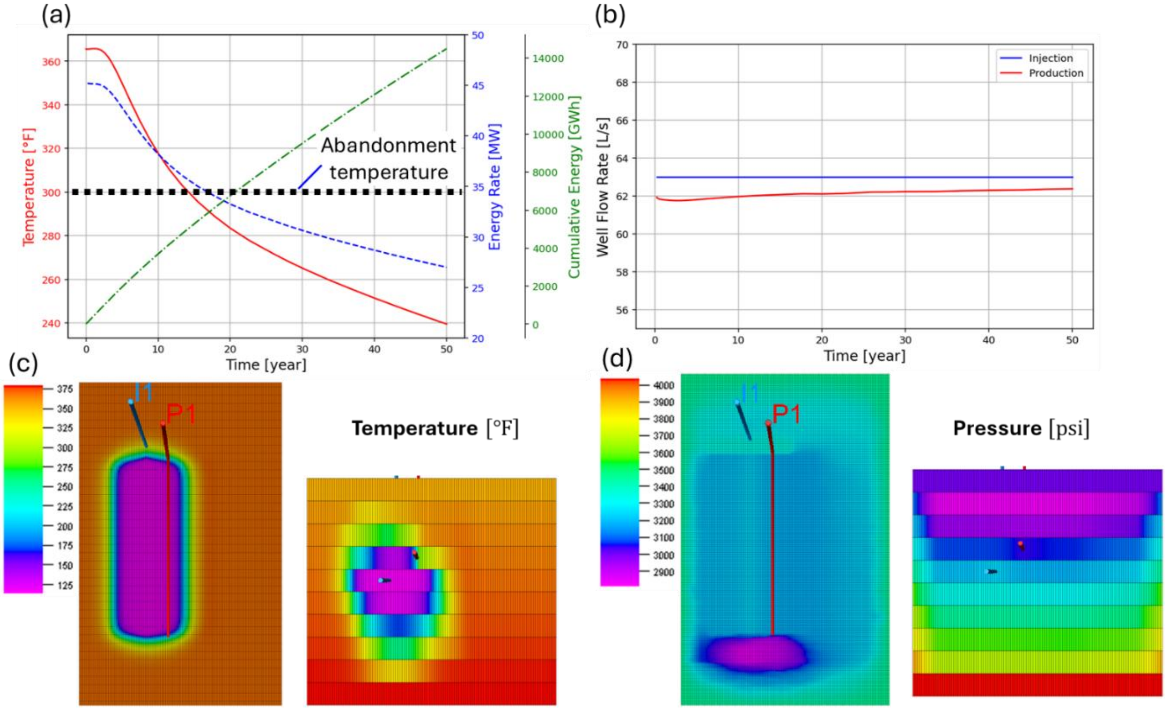

Figure 3: Simulation result of synthetic model. (a) well thermal performances including production fluid temperature, energy production rate and cumulative energy production, (b) injection and production rate, and top and gun barrel view of (c) reservoir temperature and (d) pressure after 50 years operation.

Next, we apply the proposed reduced order model, FMM-SIM, to this synthetic example. Figure 4 summarizes the application of FMM-SIM. Figure 4(a) shows the DTOF propagation in synthetic model. The FMM computes DTOF in this synthetic model requiring 0.544 seconds with 0.3 million grid cells. Based on DTOF contours, full 3D model is converted to a multi-resolution model, preserving 25 % of grid cells. Rest of the grid cells are transformed into a sequence of 1D grids and non-neighbor connections are defined using Eqs. 6 and 7. The developed multi-resolution model is validated against full 3D model as shown in Figure 4(c). We can find multi-resolution model provides almost identical well thermal performance with relative error of 1.04 %, while it accelerates reservoir simulation by a factor of 14.8.

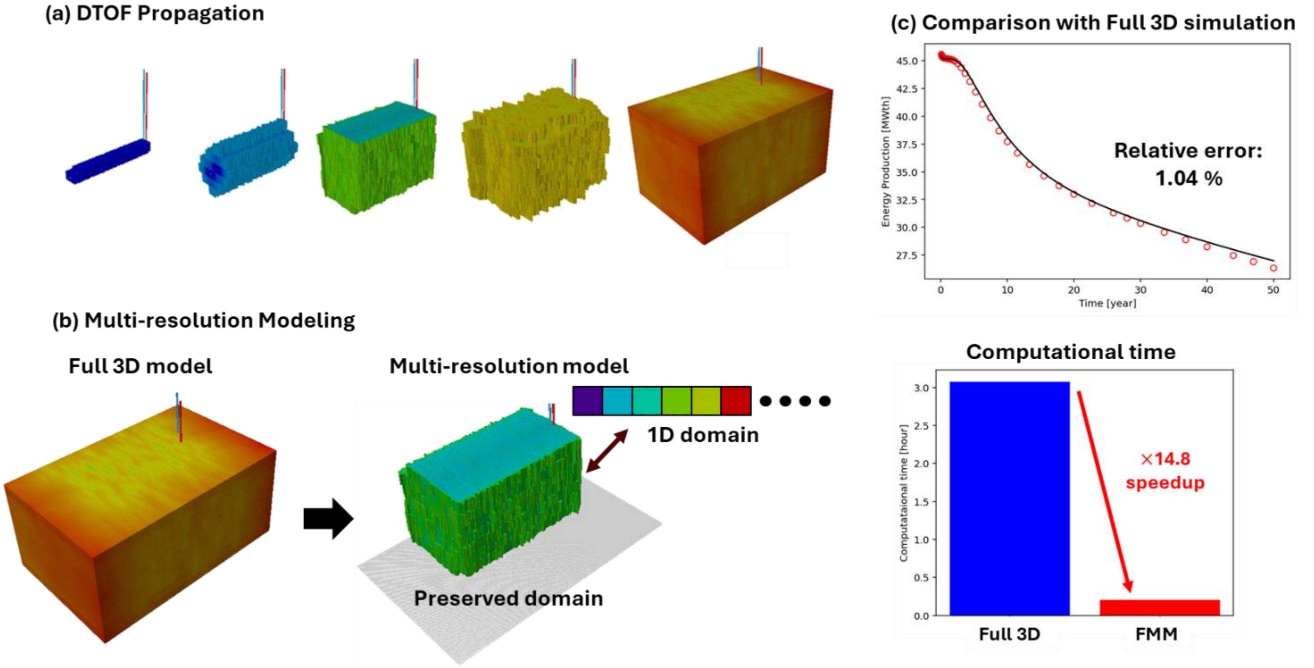

Figure 4: FMM-SIM application to the synthetic model. (a) DTOF propagation, (b) multi-resolution modeling, and (c) comparison against full 3D model in terms of energy production rate and computational time.

3.2 Effects of Connectivity, Conductivity and Conformance

Next, we investigate the effects of 3 major factors in the reservoir flow: Connectivity, Conductivity and Conformance. The connectivity indicates how the injector and producers are hydraulically connected, especially with stimulated fractures. The conductivity represents the ability of the connected pathways such as pores or fractures to transmit fluid. The conformance represents how uniformly the fluid sweeps the reservoir, which is mainly dominated by the uniformity of fracture distribution in EGS reservoir.

First, we examined the impacts of connectivity between wells. Figure 5 illustrates the reservoir simulation results in two cases: one for high connectivity which is same case as base case, and the other for lower connectivity case by removing fractures between wells. Figure 5 shows the horizontal slices where the producer located, and since we utilized FMM-SIM, only the preserved domain is visualized in Figure 5(a) and (b). Figure 5(c) compares the water production rates and temperature for the two cases and shows that the lower connectivity case exhibits a significantly reduced water production rate due to limited hydraulic connectivity. While the base case produces water with around 62 L/s, the lower connectivity case only produces around 3 L/s. Therefore, the heat energy is not effectively swept in this case, resulting in almost no cold thermal front propagation as shown in Figure 5(b). Figure 5(d) shows the cumulative energy production of two cases with different connectivity. We can see with lowering hydraulic connectivity between wells, the cumulative energy production becomes much less to 982 GWh while base case has 14460 GWh.

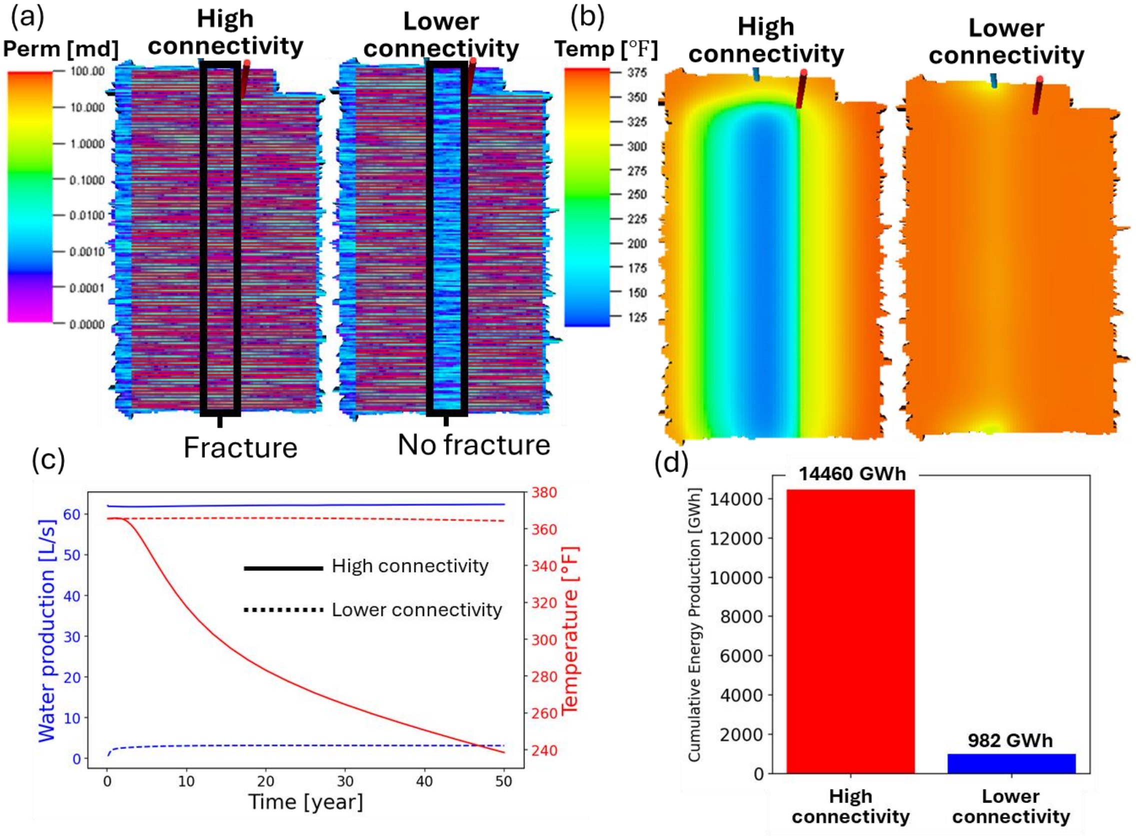

Figure 5: Parametric analysis of connectivity between wells. (a) Permeability of high and lower connectivity cases, (b) reservoir temperature after 50 years of operation, (c) water production rate and temperature behavior, and (d) cumulative energy production in two cases.

Next, we investigate the impacts of reservoir conductivity by varying the permeability of the hydraulic fractures. While the base case utilizes a fracture permeability of 100 md, the low conductivity scenario is set at 5 md. Reducing conductivity increases flow resistance, which leads to higher injection pressures. Consequently, the model more frequently encounters the bottomhole pressure (BHP) constraint at the injector. We examined two scenarios for the low conductivity case, specifically analyzing the system behavior with and without the BHP constraint.

The results are summarized in Figure 6. Referring to Figure 6(c), lower conductivity leads to a significant reduction in the water production rate. The case that includes the BHP limit shows the lowest production rate because it reaches the pressure constraint approximately 3 years of operation. These factors result in lower cumulative energy output, as illustrated in Figure 6(d). Specifically, reducing conductivity lowers cumulative energy production by 6% without pressure limits, while the addition of the BHP constraint results in a 20% reduction in cumulative energy production.

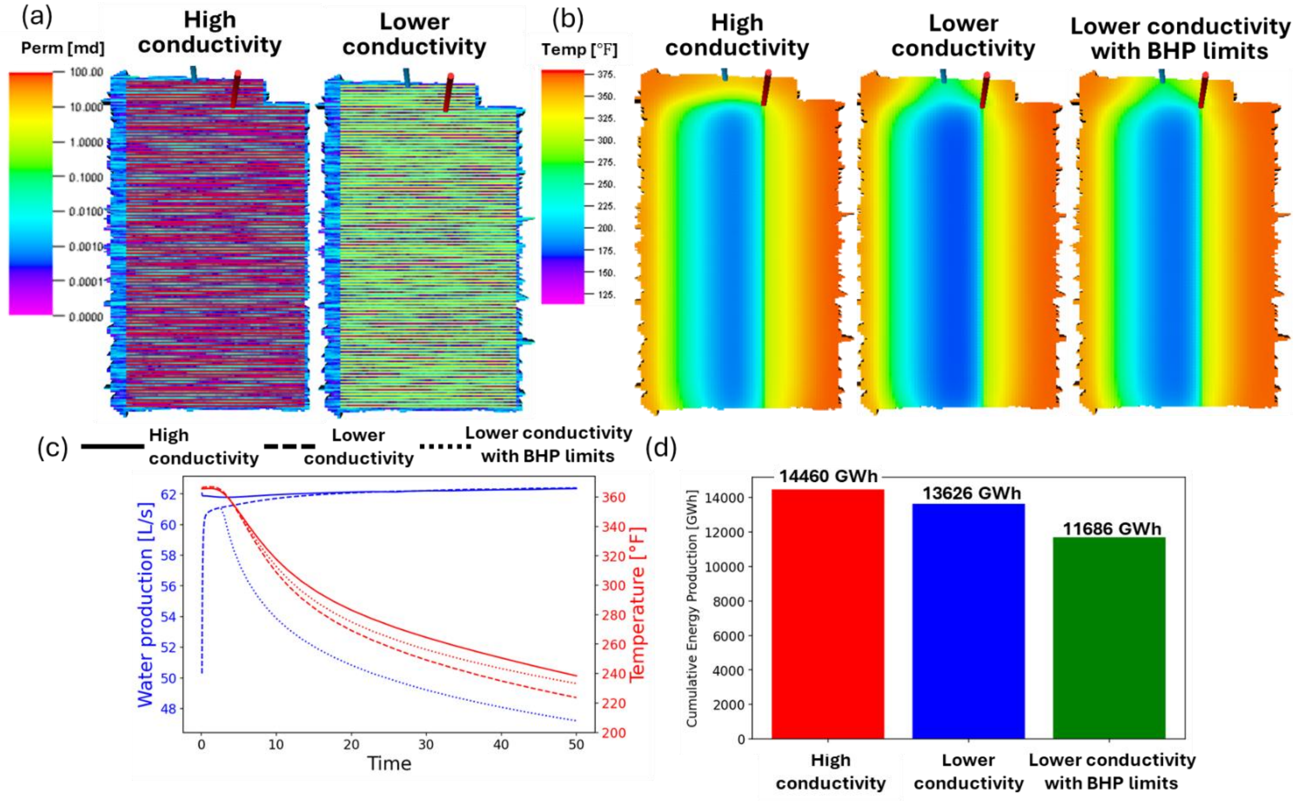

Figure 6: Parametric analysis of fracture conductivity. (a) Permeability of high and lower conductivity cases, (b) reservoir temperature after 50 years of operation, (c) water production rate and temperature behavior, and (d) cumulative energy production in three cases.

Lastly, we investigate the thermal conformance of the EGS reservoir. Conformance refers to the uniformity with which injected fluid moves through the reservoir toward the production wells. In an EGS reservoir, this property is primarily determined by the spatial distribution of the fractures. We analyzed two distinct scenarios, which include a uniform hydraulic fracture distribution and a non-uniform hydraulic fracture distribution as illustrated in Figure 7(a).

The simulation results are presented in Figure 7. Our findings indicate that reducing conformance does not significantly decrease the water production rate, but it does lead to a much sharper decline in production temperature. The reservoir temperature distribution in Figure 7(b) reveals a highly heterogeneous thermal reduction. This is caused by the non-uniformity of the stimulated fractures, which creates preferential flow paths. Although the non-uniform fracture case maintains nearly the same water production volume as the uniform case, the cumulative energy output is reduced by 10% due to the drop in production fluid temperature.

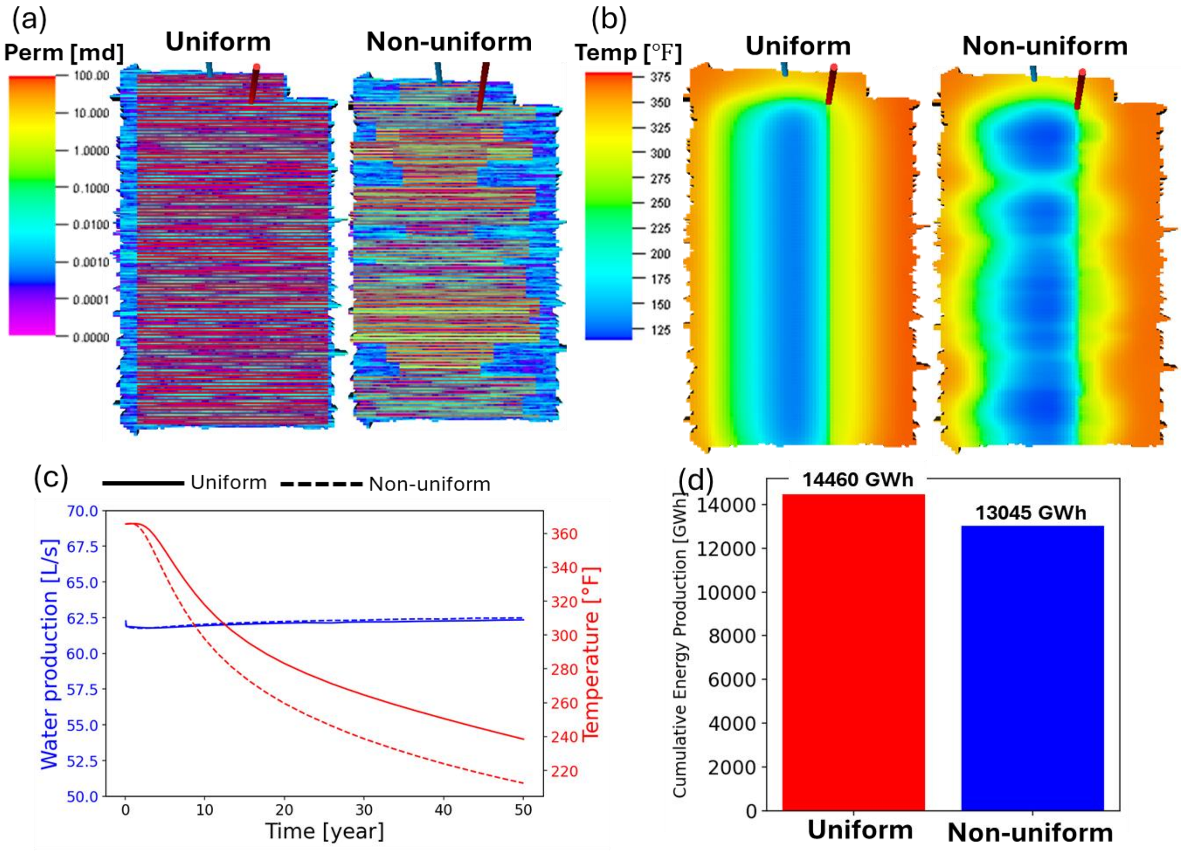

Figure 7: Parametric analysis of reservoir conformance. (a) Permeability of uniform and non-uniform fracture cases, (b) reservoir temperature after 50 years of operation, (c) water production rate and temperature behavior, and (d) cumulative energy production in two cases.

3.3 Flow-Geomechanical Coupling

To investigate the effects of geomechanical behavior in an EGS reservoir, we conducted a coupled flow and geomechanics simulation. The workflow begins with the flow module, where FMM-SIM runs the reservoir simulation to determine pressure changes within the reservoir. Based on these pressure variations, the transmissibility and pore volume multipliers are computed using Barton-Bandis model (Eqs. 9 and 10). After updating these properties to reflect the geomechanical response, the simulation proceeds to the next timestep. This update occurs at every individual timestep to ensure the coupling remains accurate.

Figure 8 presents the results of this simulation. Figure 8(a) illustrates the uniform fracture case, where pressure is reduced after 30 days of fluid circulation. Transmissibility and pore volumes decrease in response to this pressure depletion, resulting in an average transmissibility multiplier of 0.71 and a pore volume multiplier of 0.93. Figure 8(b) shows the non-uniform fracture case, which exhibits less pressure depletion because of the uneven fracture distribution. Consequently, this case maintains higher transmissibility and pore volume multipliers.

Figure 8(c) compares well performance between simulations with and without geomechanical coupling. With geomechanical effects included, the injection BHP increases by 70 psi after 50 years of operation. This rise is caused by increased flow resistance as the fractures close during pressure depletion. Conversely, the production fluid temperature changes only slightly, showing a variation of 2.56 °F. These results suggest that while geomechanical effects significantly influence the hydraulic performance of the well, their impact on the temperature behavior remains minimal.

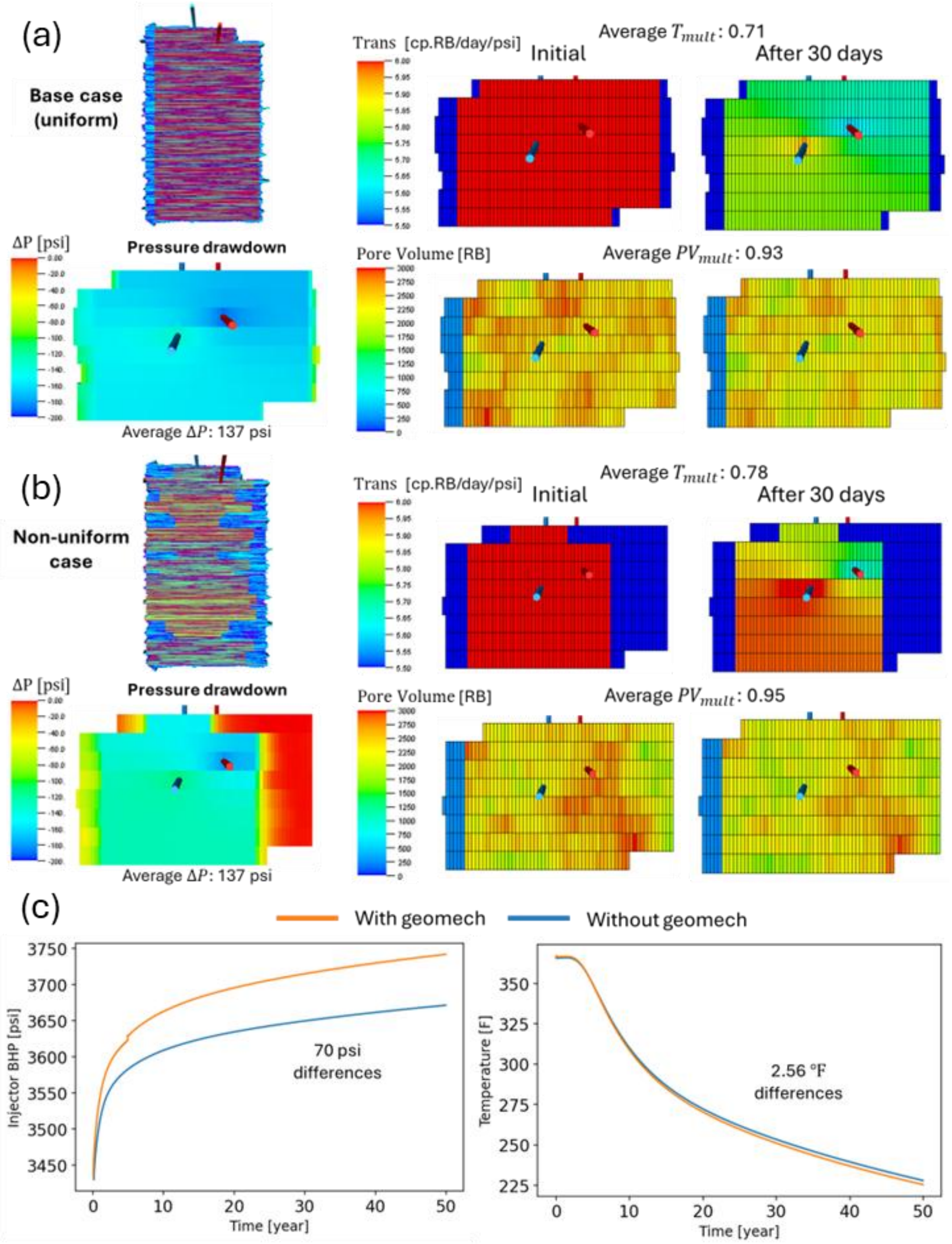

Figure 8: Result of flow-geomechanical coupling simulation. (a) Geomechanical updates in uniform fracture case, (b) geomechanical updates in non-uniform fracture case, and (c) well performance behavior in 50 years of operation

3.4 Intermittent Thermal Extraction

The developed synthetic model has open boundaries achieved by large rock and pore volume at boundary cells. During cold water injection, the cool front advances from the injector, and after the injection stops, the heat in this cooled zone gradually recovers from the surrounding rock. Figure 9(a) shows the comparison of two cases: continuous injection case and shutting wells when production temperature reached abandonment temperature (300°F). Figure 9(b) shows the reservoir temperature at the time it reached the abandonment temperature, in latter case. Observations indicate that after well shutdown, the bottomhole temperature (BHT) rises gradually as heat is recovered from the surrounding rock. Figure 9(c) shows the reservoir temperature after 50 years. After the wells were closed, the temperature in the cooled zone increased, whereas the temperature in the surrounding rock decreased. Similar to Figure 9(c), larger temperature reduction of surrounding rock was observed in lower layer due to the reason discussed in previous section (section 3.1).

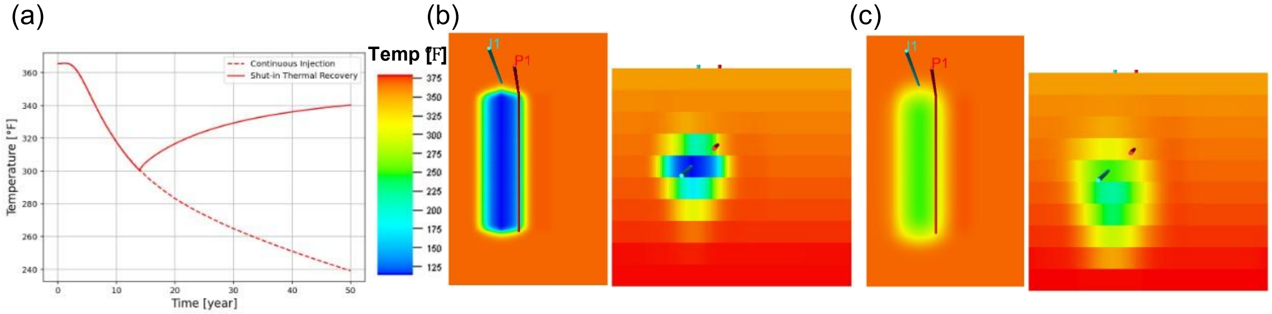

Figure 9: (a) BHT comparison between continuous injection and shutting-in, (b) reservoir temperature at abandonment temperature and (c) reservoir temperature at 50 years with shut-in

Intermittent well operation strategies are investigated to delay thermal breakthrough and maximize thermal recovery. The key controllable parameters are the durations of the injection/production operating and shut-in periods. In this study, both the injector and producer wells are opened and closed simultaneously, and the operating conditions during the production period are consistent with those used in previous applications.

Figure 10 presents a comparative analysis of different well control strategies, focusing on the impact of cycle duration in intermittent operations. Cycle lengths were modeled from 0.5 to 4 years, ensuring equal durations for the operation and shut-in phases. All simulations were terminated once the production fluid temperature declined to the specified abandonment threshold (300°F). As depicted in Figure 10(a), the intermittent strategies induce periodic fluctuations in BHT, correlating directly with cyclic operation. A distinct thermal buildup is evident during the shut-in periods. However, these localized variations do not alter the global trend; the overall temperature decline profiles are remarkably similar for all cases in Figure 10(a). As a result, the abandonment temperature is reached at a comparable operational time across all simulated strategies. This trend is mirrored in cumulative energy production, shown in Figure 10(b). The intermittent cases produce cumulative energy outputs that are nearly identical among them. The minor, short-term deviations associated with cyclic frequency have a negligible effect on the total energy extracted over the lifetime of the well.

Figure 10(c) and (d) present the results of an analysis wherein the operation (open) and shut-in (close) durations were asymmetrical. In this investigation, the ratio of open to shut-in durations was systematically varied, specifically comparing 2:1, 1:1, and 1:2 year cycles. These variations resulted in a clear differentiation between the observed thermal profiles. As the duration of the shut-in period increases relative to the production period, the rate of temperature reduction becomes milder. This mitigation of thermal decline results in a longer operational time before the abandonment temperature is reached. For example, the scenario utilizing a 1-year open phase and a 2-year shut-in phase (a 1:2 ratio) achieves an operational lifespan of 73 years. This is around 5 times longer than continuous injection case. Referring to Figure 10(d), this extended operational longevity directly correlates with a larger ultimate energy recovery, indicating that longer recharge periods enhance total energy recovery over the well's lifetime.

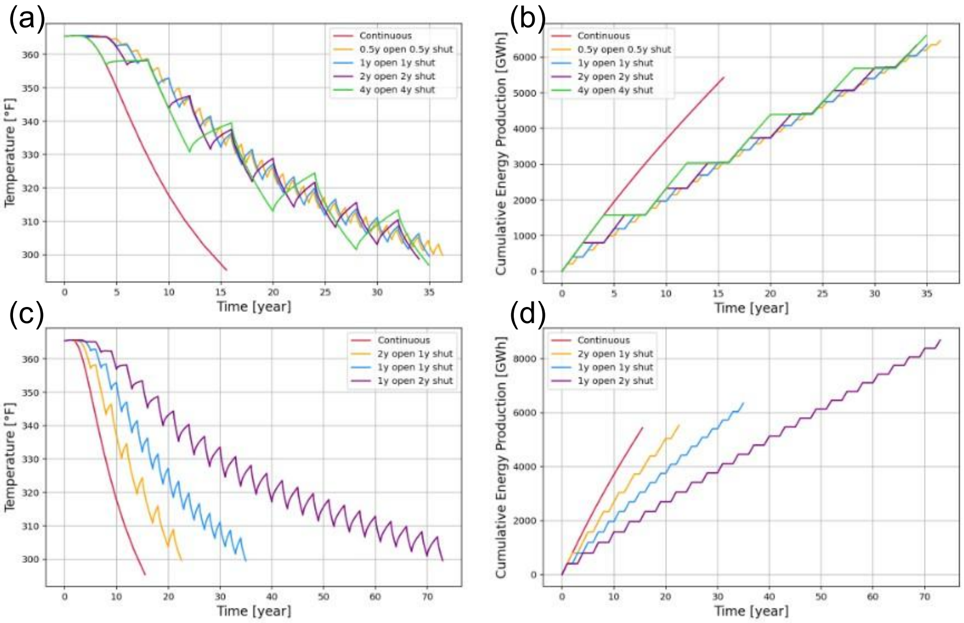

Figure 10: Result of intermittent well control strategies. (a) temperature and (b) cumulative energy production by changing cycle length, and (c) temperature and (d) cumulative energy production by changing ratio of operating and closing period.

Figure 10 demonstrates that the ratio of open to shut duration is a key parameter in the intermittent operation strategy. While a longer shut-in period yields higher cumulative energy production, it also results in a lower production rate due to the non-producing intervals. This indicates a trade-off between ultimate energy output and energy production rate. A further investigation is therefore conducted to analyze this trade-off by changing operational ratio, defined as the ratio of operating duration to shut-in duration.

Figure 11 presents the comparison between different operational ratios. The cycle length is fixed at 2 years, and an operational ratio of 0.1 indicates that the wells operate 10% of each cycle and remain shut for the rest of the period. As the operational ratio decreases, meaning longer shut-in durations, the temperature decline becomes slower, resulting in higher ultimate cumulative energy production as shown in Figure 11(a) and (b). However, this also corresponds to a lower energy production rate due to non-producing period. Because the simulation is limited to 100 years, some cases (operational ratios of 0.1 and 0.2) do not reach the abandonment temperature.

Figure 11 illustrates the relationship between the average energy production rate and the ultimate cumulative energy production. The average energy production rate is calculated by dividing the ultimate cumulative energy production by the time required to reach the abandonment temperature. The cases with operational ratio (OR) = 0.1 and 0.2 are considered outliers because they did not reach the abandonment temperature. Excluding these two cases, a systematic relationship is observed between the average production rate and the cumulative energy output. Higher production rates correspond to lower ultimate energy recovery. Detailed analysis indicates a roughly linear trend at higher operational ratios. As shown in Figure 11, for OR values between 0.6 and 1.0, the average energy production rate and ultimate energy recovery exhibit a linear correlation as follows. This equation can be applied to determine the appropriate well control conditions in the model. It should be noted, however, that the coefficients in Eq. 11 may vary depending on specific model parameters such as injection rate, number of stimulated intervals, and lateral length.

$$\text{Ultimate Energy Recovery [GWh]} = -56.75 \cdot \text{Average Energy Production Rate [MW]} + 7109.18 \tag{11}$$

Conversely, for OR ≤ 0.5, the results deviate from Eq. 11, particularly in cases with higher ultimate energy recovery. This deviation indicates a nonlinear trend, particularly an exponential increase in ultimate energy recovery. This observation suggests that a specific operational ratio can balance the heat replenishment rate in the subsurface and the energy extraction rate, enabling completely sustainable heat extraction. In this study, the maximum simulation time is set to 100 years, and within this period, such an equilibrium point was not observed.

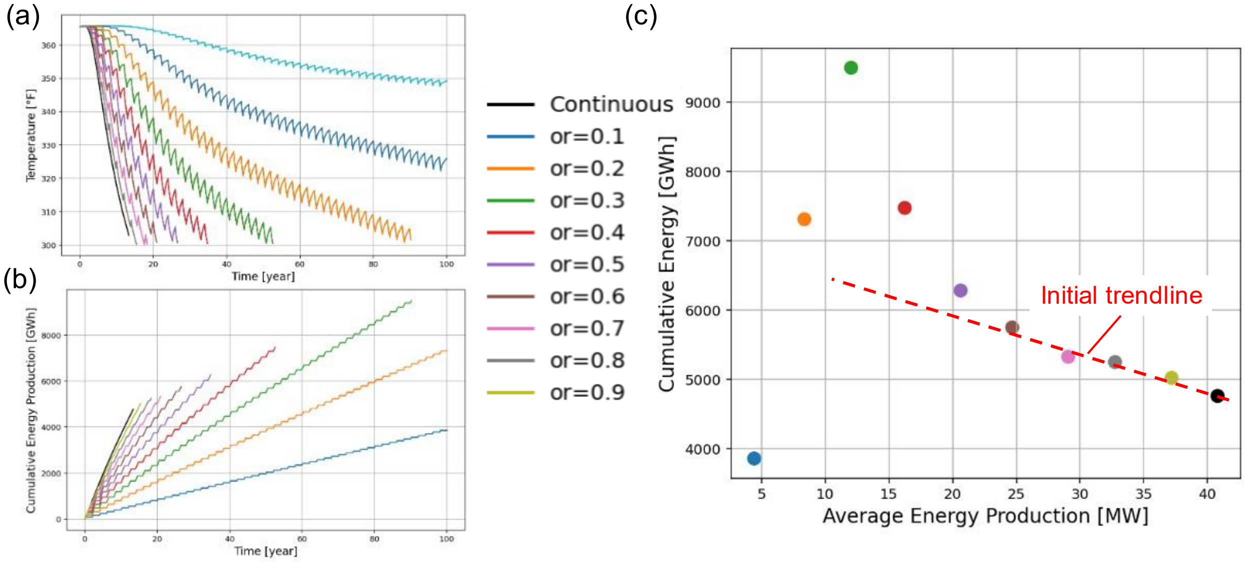

Figure 11: Thermal performance with different operation ratio. (a) Temperature profile, (b) cumulative energy production, and (c) average energy production rate vs. ultimate cumulative energy production

4. UTAH FORGE APPLICATION

The initial dynamic reservoir modeling in Utah FORGE site was carried out by Chan, Kumawat, et al. (2025). This work extends this previous work to improve history matching performance with geomechanical coupling and attempts to optimize the well control to delay thermal breakthrough.

4.1 Prior Reservoir Modeling

Our dynamic reservoir model integrates a Discrete Fracture Network (DFN), a native-state model, fiber-optic Distributed Strain Sensing (DSS) measurements, and field responses from a one-month fluid circulation test. The workflow begins with a prior model, where the DFN model (Finnila & Jones, 2024) defines the geological framework and the native-state model (Podgorney, 2020) establishes initial physical conditions. The resulting prior reservoir model is illustrated in Figure 12.

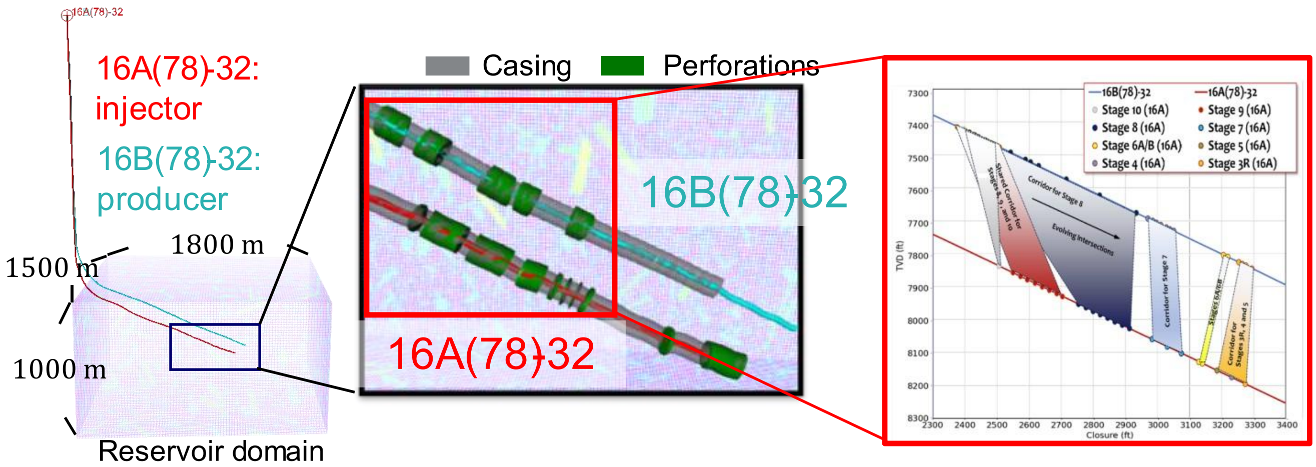

Figure 12: Prior reservoir model with fracture corridors. Figures of fracture corridors after Kumawat et al. (2025).

Preliminary simulations indicated that this prior model failed to provide sufficient hydraulic connectivity between the injector and producer. This discrepancy suggests that the reference DFN does not adequately represent the hydraulically stimulated fractures. To resolve this, we updated the DFN using DSS measurements, which identify "fracture hits" by monitoring spatio-temporal strain variations along the wellbore. As a hydraulic fracture approaches or intersects the monitoring well, it induces localized stress-field changes, typically observed as sudden signal shifts. By applying signal processing to detect these micro-deformations and correlating them with injection timing and depth, we can infer fracture propagation paths with high spatial resolution.

At the Utah FORGE site, DSS fiber is installed in the producer, well 16B(78)-32, and strain changes are recorded during stimulation (Jurick, 2024). Utilizing this data, Kumawat et al. (2025) identified fracture corridors, which are the zones with a high probability of containing stimulated fractures (Figure 12). These corridors were mapped by linking specific fracturing stages in the injector to corresponding stress responses in the producer. To reflect this enhanced connectivity in the simulation, we assigned permeability and porosity multipliers within these identified zones, which are subsequently calibrated during the history-matching phase.

The integration of geological, petrophysical, and structural models is performed using PETREL^{TM} (SLB, 2024b) a comprehensive subsurface modeling platform. The reservoir simulation deck is subsequently constructed and exported to the ECLIPSE^{TM} Compositional Simulator (E300) (SLB, 2024a) with the thermal option, allowing for fully coupled thermal and compositional flow simulations.

4.2 FMM-SIM Application to Utah FORGE Model

To accelerate the reservoir simulation, FMM-SIM was applied to the prior model. The FMM computed the DTOF for this 2.7 million cell grid in only 5.83 seconds. The resulting DTOF distribution, shown in Figure 13(a), illustrates the pressure front propagation within the Utah FORGE reservoir. Using these DTOF contours, we constructed a multi-resolution model. This approach preserves the original 3D cells near the wellbore while transforming the distal regions into an efficient 1D grid. A DTOF threshold was applied to distinguish between these domains, specifically calibrated to retain 20% of the original grid cells in the high-resolution wellbore region as shown in Figure 13(b).

The FMM-SIM multi-resolution model was validated against the full 3D simulation, yielding nearly identical well responses as shown in Figure 13(c). Relative errors were negligible, which are 0.1% for production BHP and 0.0009% for production fluid temperature. As shown in Figure 13(d), this method achieved a 14.1x speedup. While the full 3D model required 14.7 hours per run, the FMM-SIM model completed in just 1.04 hours, significantly enhancing the efficiency of the history-matching process while preserving the estimation accuracy.

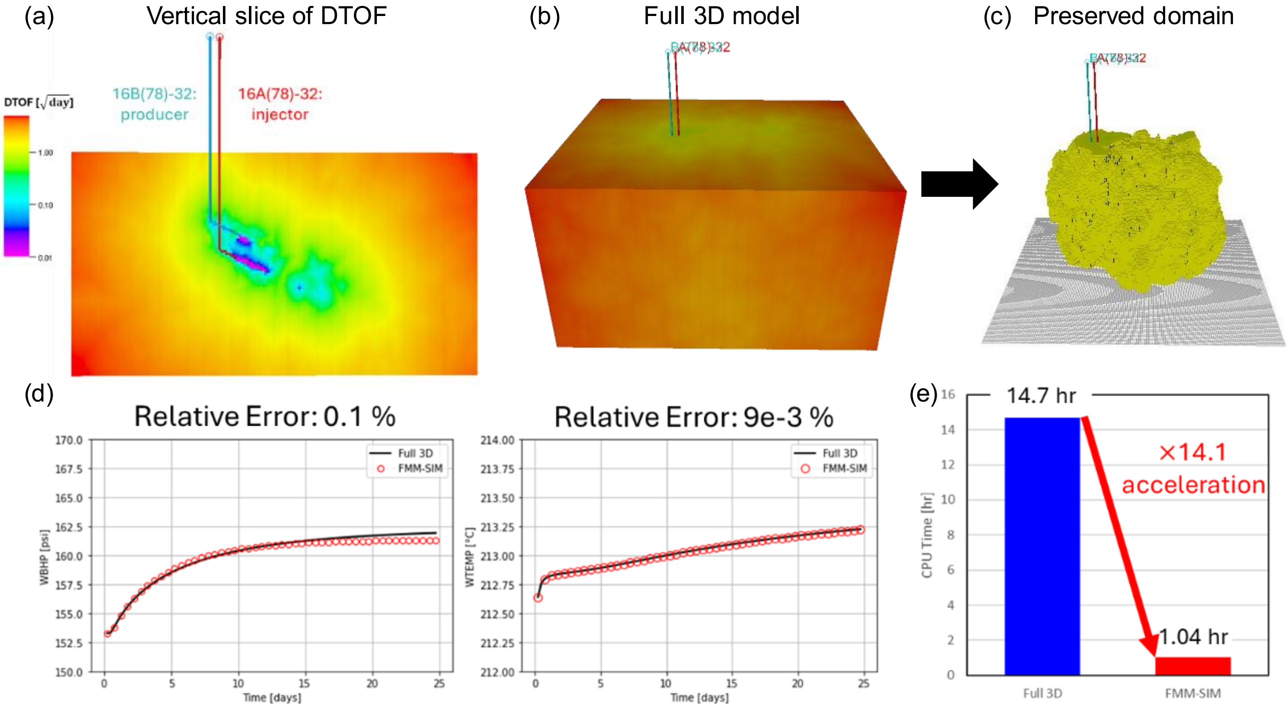

Figure 13: (a) Vertical slice of DTOF distribution, (b) full 3D model, (c) preserved domain in multi-resolution model (d) performance comparison on BHP and production fluid temperature and (e) required computational time. Figures from Chan, Kumawat, et al. (2025)

4.3 History Matching

Utilizing the accelerated FMM-SIM model, history matching was performed to calibrate the prior reservoir model by assimilating the field-observed well responses as illustrated in Figure 14. BHP for both the injector and producer was derived from measured tubing head pressure, accounting for hydrostatic head and frictional losses (Kumawat et al., 2025). Well controls were defined by field-observed flow rates, with calibration targets including BHP for both wells and production fluid temperatures, forming a three-objective optimization problem.

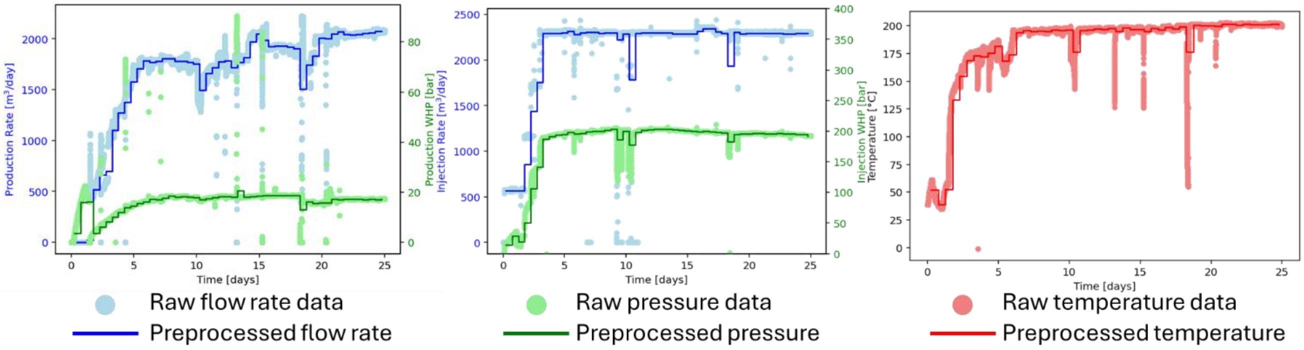

Figure 14: Field observed data in one month circulation test. Data is visualized based on McLennan et al. (2024).

Data assimilation was conducted using a Multi-Objective Genetic Algorithm (MOGA). We utilized Non-dominated Sorting Genetic Algorithm II (NSGA-II) proposed by Deb et al. (2002). We run MOGA with a population size of 80 over 10 generations. The calibration parameters are summarized in Table 1. The parameters included well index multipliers for both wells and permeability/porosity multipliers for the fracture corridors.

Table 1: Optimization parameters

Parameter	Min value	Max value
Well index multiplier for injector	0.5	5
Well index multiplier for producer	0.5	5
Permeability multiplier for fracture corridor	10	1000
Porosity multiplier for fracture corridor	1	20

The history matching results are summarized in Figure 15. As shown in Figure 15(a), production fluid temperature remained nearly constant across all realizations. This suggests that over the one-month historical period, temperature exhibits low sensitivity to the selected parameter variations. While these parameters were intended to calibrate the flow profile, the short historical duration makes thermal breakthrough differences difficult to resolve. In contrast, injection and production BHPs showed significant variation. The Pareto-optimal cases, highlighted in blue, demonstrate a significantly closer match to field observations than the initial realizations.

Figure 15(b) illustrates the objective function values of evaluated cases. Given the minimal sensitivity of production temperature, the results are visualized as a two-dimensional projection of injection BHP versus production BHP. A well-defined Pareto front is evident in this objective space. Finally, Figure 15(c) depicts the evolution of parameter distributions. The narrowing of these ranges from the initial generation to the Pareto-optimal set indicates successful convergence. Notably, the Pareto front retains a degree of parameter variability, which is essential for characterizing uncertainty and ensuring robust future forecasting.

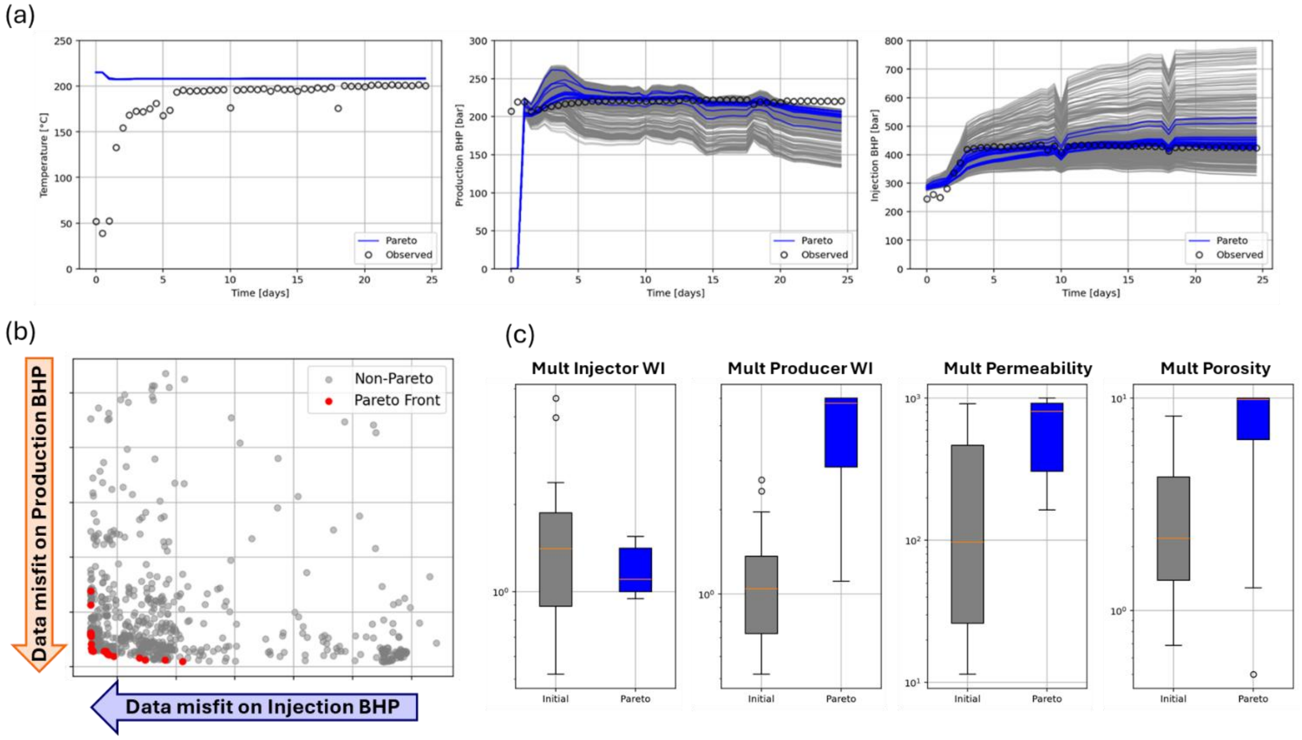

Figure 15: History matching results. (a) Well responses, (b) objective function value plot, and (c) parameter distribution changes from initial generation to pareto front.

Subsequently, the history matching results were refined by implementing a geomechanical module. Figure 16(a) illustrates one of the optimized cases selected from the previous analysis. A key discrepancy was observed in the late-time production BHP highlighted by red dashed circle: while the field-observed data remained relatively stable, the initial simulation results exhibited a distinct declining trend. To address this discrepancy, the geomechanical module was coupled with following parameters: $k_{rf} = 0.5, K_n = 1, w_{init} = 0.2, c_{pp} = 5$. The implementation of geomechanical coupling successfully corrected this trend, maintaining a more constant production BHP that aligns with field observations. This improvement is attributed to the geomechanical response to pressure depletion near the producer. As pore pressure decreases, the effective stress on the fractures increases, leading to fracture closure. This reduction in fracture aperture increases flow resistance near the wellbore, which stabilizes the BHP. In contrast, the uncoupled model fails to account for this dynamic permeability reduction, resulting in the erroneous pressure decline. This finding strongly suggests that fracture closure is occurring in the field and underscores the necessity of considering geomechanical behavior to achieve an accurate history match.

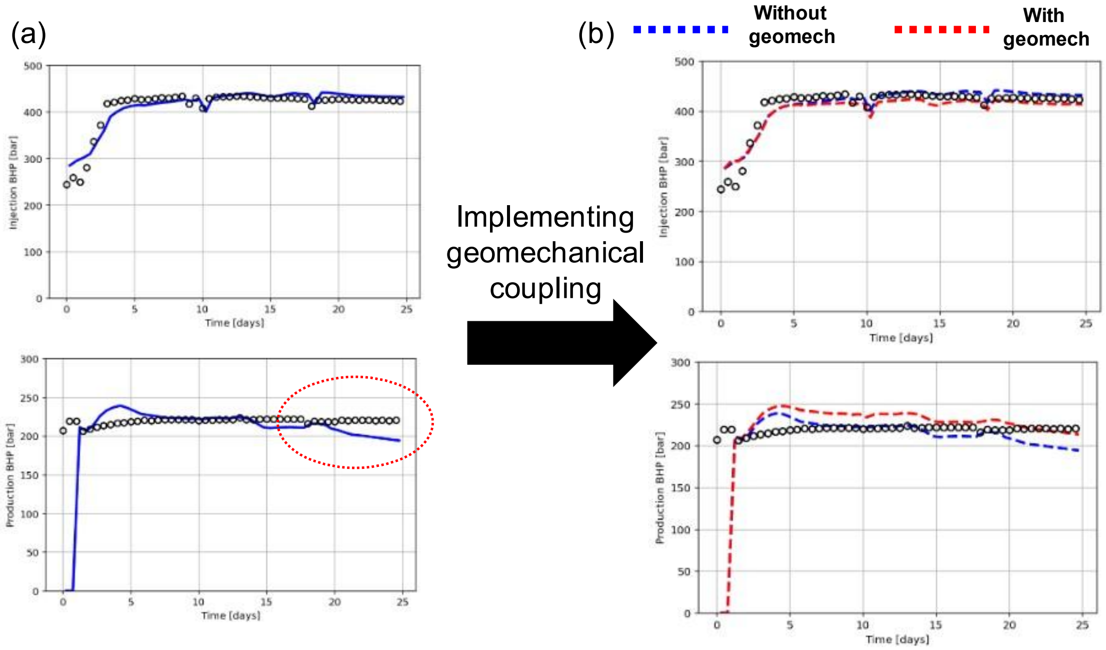

Figure 16: History matching implementing geomechanical coupling. (a) Well performance before geomechanical coupling and (b) those after geomechanical coupling

4.4 Optimizing Well Control Thorough Intermittent Thermal Extraction

Using the calibrated reservoir model, we investigated an intermittent thermal extraction strategy at the Utah FORGE site to evaluate how Operational Ratio (OR) influences thermal recovery efficiency. Five ratios were tested: OR = 0.2, 0.4, 0.6, 0.8, and 1.0 (continuous operating). The results are illustrated in Figure 17. As shown in Figure 17(a), which plots the completion cell temperature and cumulative energy production, the reservoir temperature exhibits significant recovery during shut-in periods. Using an abandonment temperature threshold of 120°C, the data demonstrates that lower operational ratios result in higher cumulative energy production. This increase is primarily attributed to the retardation of thermal breakthrough, allowing for a more sustained heat extraction profile.

Figure 17(b) highlights the trade-off between the average energy production rate and cumulative energy production. While reducing the operational ratio delays thermal breakthrough and maximizes the total energy production, it simultaneously lowers the average production rate due to the extended shut-in durations. This analysis suggests that the optimal OR must be selected by balancing the requirement for long-term reservoir longevity against the need for immediate energy output.

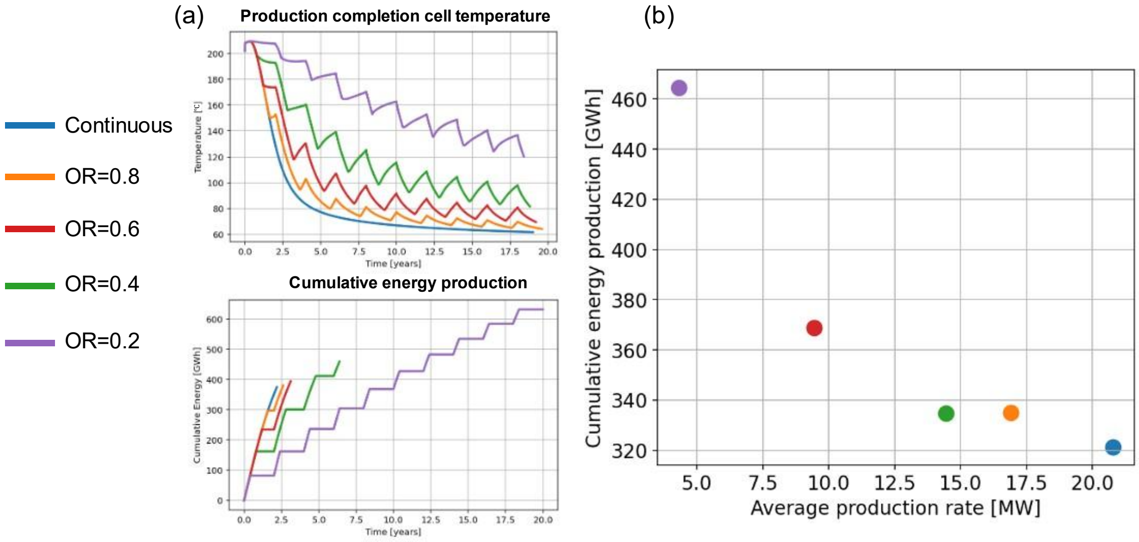

Figure 17: Optimization result by intermittent thermal extraction at the Utah FORGE site. (a) Completion cell temperature and cumulative energy production, (b) illustration of cumulative energy production against average production rate

5. CONCLUSION

We have presented a comprehensive sensitivity analysis and dynamic reservoir modeling in EGS projects using Fast Marching-based reservoir simulation. By utilizing the FMM-SIM reduced-order modeling approach, we achieved over an order of magnitude improvement in computational efficiency compared to Full 3D simulation with minimal loss in accuracy. This acceleration enabled a detailed investigation into the influential 3 major parameters (connectivity, conductivity, and conformance) alongside geomechanical and well-control effects on thermal breakthrough. These findings were then successfully applied to the Utah FORGE site for data assimilation and the optimization of extraction strategies.

Our key results from this paper are summarized as follows:

- Using a synthetic model designed after a commercial-scale EGS project, we quantified the influence of reservoir connectivity, conductivity, and conformance on thermal energy production. The results confirm that optimizing all three "C" components simultaneously is essential for maximizing thermal recovery and delaying premature heat breakthrough.

- We integrated the Barton-Bandis model with the FMM-SIM flow simulator to account for fracture closure. Our analysis demonstrates that geomechanical effects significantly influence pressure behavior, specifically by increasing flow resistance as fractures close, while having a more subtle impact on thermal profiles.

- Sensitivity analysis of intermittent thermal extraction revealed that the Operational Ratio, defined as the balance of production versus shut-in time, is the primary determinant of recovery efficiency. Lowering the ratio retards thermal breakthrough but requires a trade-off with immediate power output.

- A high-fidelity dynamic model was constructed by synthesizing the reference DFN, native state initial conditions, and Distributed Strain Sensing data. This integration allowed us to characterize stimulated fracture configurations with high spatial resolution using field observed responses.

- The FMM-SIM approach accelerated the Utah FORGE reservoir simulation by a factor of 14.7. Despite this significant speedup, the model maintained accuracy, yielding relative errors of only 0.1% for BHP and 0.009% for production temperature compared to full 3D simulations.

- Leveraging the Multi-Objective Genetic Algorithm (MOGA), we performed history matching of the Utah FORGE site incorporating geomechanical coupling. This improved the match with field data and suggested that fracture closure is a likely phenomenon at the field site. The resulting calibrated model provides a robust tool for balancing long term reservoir longevity with immediate energy demands through optimized well control strategies.

REFERENCES

Al Balushi, F., Zhang, Q., and Dahi Taleghani, A.: Autonomous Fracture Conductivity Using Expandable Proppants in Enhanced Geothermal Systems, *SPE Journal*, *28*(05), (2023), 2660-2674. https://doi.org/10.2118/215823-pa

Augustine, C., Fisher, S., Ho, J., Warren, I., and Witter, E. (2023). *Enhanced Geothermal Shot Analysis for the Geothermal Technologies Office*. https://www.osti.gov/biblio/1922621

Barton, N., Bandis, S., and Bakhtar, K.: Strength, deformation and conductivity coupling of rock joints, *International Journal of Rock Mechanics and Mining Sciences & Geomechanics Abstracts*, *22*(3), (1985), 121-140. https://doi.org/https://doi.org/10.1016/0148-9062(85)93227-9

Chan, C.-H., Datta-Gupta, A., and Shor, R. J.: Fast Marching Method: A New Paradigm for Rapid Simulation of Enhanced Geothermal Systems, Proceedings of the 50th Workshop on Geothermal Reservoir Engineering, Stanford University, Stanford, California, February, (2025).

Chan, C.-H., Datta-Gupta, A., and Shor, R. J.: Fast Marching Method: A new paradigm for rapid simulation of enhanced geothermal systems, *Geoenergy Science and Engineering*, *257*, (2026), 214257. https://doi.org/https://doi.org/10.1016/j.geoen.2025.214257

Chan, C.-H., Kumawat, P. K., Deo, M., and Datta-Gupta, A.: Dynamic Reservoir Modeling of the Utah FORGE Enhanced Geothermal Project Using Fast Marching Method, SPE Energy Transition Symposium, (2025). https://doi.org/10.2118/228338-ms

Chan, C.-H., Onishi, T., Datta-Gupta, A., Esmaeilpour, M., and Saar, M. O.: Rapid Multi-Domain Multi-Resolution Simulation of CO_2-based Enhanced Geothermal Systems, European Gothermal Congress 2025, Zurich, Switzerland (2025, October 6-10, 2025).

Chen, H., Li, A., Terada, K., and Datta-Gupta, A.: Rapid Simulation of Unconventional Reservoirs by Multidomain Multiresolution Modeling Based on the Diffusive Time of Flight, *SPE Journal*, *28*(03), (2023), 1083-1096. https://doi.org/10.2118/214308-pa

Chen, H., Onishi, T., Park, J., and Datta-Gupta, A.: Computing Pressure Front Propagation Using the Diffusive-Time-of-Flight in Structured and Unstructured Grid Systems via the Fast-Marching Method, *SPE Journal*, *26*(03), (2021), 1366-1386. https://doi.org/10.2118/201771-pa

Cong, L., Lu, S., Jiang, P., Zheng, T., Yu, Z., and Lü, X.: Research Progress on CO2 as Geothermal Working Fluid: A Review, *Energies*, *17*(21), (2024), 5415. https://www.mdpi.com/1996-1073/17/21/5415

Datta-Gupta, A., and King, M. (2007). *Streamline Simulation: Theory and Practice* (Vol. 11). https://doi.org/10.2118/9781555631116

Datta-Gupta, A., Kulkarni, K. N., Yoon, S., and Vasco, D.: Streamlines, ray tracing and production tomography: Generalization to compressible flow, *Petroleum Geoscience, 7, SUPP*, *75*(86), (2001), 12.

Datta-Gupta, A., Xie, J., Gupta, N., King, M. J., and Lee, W. J.: Radius of Investigation and its Generalization to Unconventional Reservoirs, *Journal of Petroleum Technology*, *63*(07), (2011), 52-55. https://doi.org/10.2118/0711-0052-jpt

Davies, J. P., and Davies, D. K.: Stress-Dependent Permeability: Characterization and Modeling, *SPE Journal*, *6*(02), (2001), 224-235. https://doi.org/10.2118/71750-pa

Deb, K., Pratap, A., Agarwal, S., and Meyarivan, T.: A fast and elitist multiobjective genetic algorithm: NSGA-II, *IEEE Transactions on Evolutionary Computation*, *6*(2), (2002), 182-197. https://doi.org/10.1109/4235.996017

Dehdouh, A., Mellal, I., Bettir, N., Abdelhamid, C., Allam, L., Rasouli, V., and Gyimah, E.: Key Design Parameters for Enhanced Geothermal System (EGS), 58th U.S. Rock Mechanics/Geomechanics Symposium, (2024). https://doi.org/10.56952/arma-2024-0894

Finnila, A., and Jones, C.: *Utah FORGE: 2024 Discrete Fracture Network Model Data* Energy and Geoscience Institute at the University of Utah, (2024). https://doi.org/10.15121/2440870

Horne, R., Genter, A., McClure, M., Ellsworth, W., Norbeck, J., and Schill, E.: Enhanced geothermal systems for clean firm energy generation, *Nature Reviews Clean Technology*, *1*(2), (2025), 148-160. https://doi.org/10.1038/s44359-024-00019-9

Jurick, D.: *Utah FORGE: Well 16B(78)-32 DTS, RFS DSS Strain, and Absolute Strain Circulation Test Fiber Optic Data - August 2024* Neubrex Energy Services (US), LLC, (2024). https://doi.org/10.15121/2531108

Kumawat, P. K., Panja, P., Jin, W., Munday, L. B., Podgorney, R., Earnest, E., Upchurch, E. R., Tozzi, M., Deo, M., and McLennan, J.: Simplified Fracture Model for Numerical Simulation of EGS: A Utah FORGE Case Study, Proceedings of the 50th Workshop on Geothermal Reservoir Engineering, Stanford University, Stanford, California, February, (2025).

Liu, S., Ji, K., and Jin, M.: Review of Techniques to Mitigate Thermal Breakthrough in Enhanced Geothermal Systems. In *Preprints*: Preprints. (2025).

McLennan, J., England, K., and Swearingen, L.: *Utah FORGE: Wells 16A(78)-32 and 16B(78)-32 Extended Circulation Test Data - August and September 2024* Energy and Geoscience Institute at the University of Utah, (2024). https://doi.org/10.15121/2475065

Moore, J., and McLennan, J. D.: An Overview of the Utah Frontier Observatory for Research in Geothermal Energy (FORGE), AGU Fall Meeting Abstracts, (2018).

Norbeck, J., Gradl, C., and Latimer, T. (2024). Deployment of Enhanced Geothermal System technology leads to rapid cost reductions and performance improvements. X5VH8C. Retrieved September 01, 2024, from https://ui.adsabs.harvard.edu/abs/2024EaArX...X5VH8CN

Norbeck, J., and Latimer, T. (2023). Commercial-Scale Demonstration of a First-of-a-Kind Enhanced Geothermal System. X52X50B. Retrieved July 01, 2023, from https://ui.adsabs.harvard.edu/abs/2023EaArX...X52X0BN

Park, J., Iino, A., Datta-Gupta, A., Bi, J., and Sankaran, S.: Rapid Modeling of Injection and Production Phases of Hydraulically Fractured Shale Wells Using the Fast Marching Method, SPE/AAPG/SEG Unconventional Resources Technology Conference, (2019). https://doi.org/10.15530/urtec-2019-339

Podgorney, R.: *Utah FORGE: Data for 3-D Model Development - Lithology, Temperature, Pressure, and Stress* Idaho National Laboratory, (2020). https://doi.org/10.15121/1605155

Rutqvist, J., and Tsang, C.-F.: A study of caprock hydromechanical changes associated with CO2-injection into a brine formation, *Environmental Geology*, *42*(2), (2002), 296-305. https://doi.org/10.1007/s00254-001-0499-2

Sethian, J. A.: A fast marching level set method for monotonically advancing fronts, *Proceedings of the National Academy of Sciences*, *93*(4), (1996), 1591-1595. https://doi.org/doi:10.1073/pnas.93.4.1591

Sethian, J. A.: Fast Marching Methods, *SIAM Review*, *41*(2), (1999), 199-235. https://doi.org/10.1137/s0036144598347059

SLB. ECLIPSE Reservoir Simulator. In (Vol. 2024). Houston, TX: SLB. (2024a).

SLB. Petrel subsurface software. In (Vol. 2024). Houston, TX: SLB. (2024b).

Smith, T., Shukla, P., Mukku, V., Cortez, O., Tang, B., and Sharan, S. (2025). *Enhanced Geothermal Systems Modeling and Optimization Workflows for Power Production from Geothermal Reservoirs*. https://doi.org/10.2118/228334-MS

Terrell, M. (2021). With new geothermal project, it's full steam ahead for 24/7 carbon-free energy. Retrieved May 19, from https://cloud.google.com/blog/products/infrastructure/google-fervo-geothermal-project-creates-carbon-free-energy

Vasco, D. W., Keers, H., and Karasaki, K.: Estimation of reservoir properties using transient pressure data: An asymptotic approach, *Water Resources Research*, *36*(12), (2000), 3447-3465. https://doi.org/https://doi.org/10.1029/2000WR900179

Virieux, J., Flores-Luna, C., and Gibert, D.: Asymptotic Theory For Diffusive Electromagnetic Imaging, *Geophysical Journal International*, *119*(3), (1994), 857-868. https://doi.org/10.1111/j.1365-246X.1994.tb04022.x

Wu, Y.-S., Li, J., Ding, D.-Y., Wang, C., and Di, Y.: A Generalized Framework Model for the Simulation of Gas Production in Unconventional Gas Reservoirs, *SPE Journal*, *19*(05), (2014), 845-857. https://doi.org/10.2118/163609-pa

APPENDIX

Appendix A. Modeling of A Commercial-scale EGS Project

A reservoir simulation model referring to a commercial-scale EGS project was developed in this work. This model is based on Project Red site operated by Fervo Energy. Project Red is a geothermal development located in northern Nevada, proximate to the existing Blue Mountain power facility. The project involved design, drilling, and stimulation. This system consists of two horizontal wells, configured as an injection-production doublet, and one deep vertical well for reservoir monitoring. Field operations were conducted in phases: the drilling and stimulation campaign occurred from January 2022 to March 2023, with subsequent well testing completed between April and May 2023. The technical framework for power conversion assumes the utilization of an air-cooled organic Rankine cycle (ORC) plant.

Figure A - 1 shows top and cross-section view of project Red site. Around 3,000 ft horizontal injector (Well 34A-22) and producer (Well 34-22) were stimulated using a 16-stage plug-and-perforate methodology. The injector was completed with 102 perforation clusters and the producer with 94, both at an average 30 ft spacing. Data from in-well fiber optic sensors confirmed successful fracture breakdown and initiation at 100% of the clusters. A subsequent 30-day standard geothermal well test achieved a high-temperature flow rate of 63 L/s, demonstrating a potential electrical production capacity of 3.5 MW (Norbeck & Latimer, 2023).

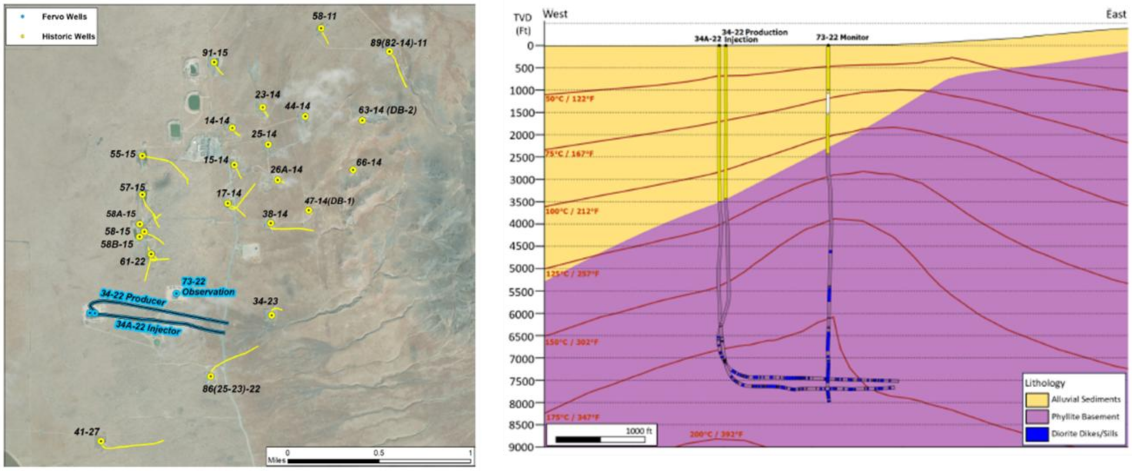

Figure A - 1: Top and cross-section view of project Red site (Norbeck & Latimer, 2023)

The first step of reservoir modeling is delineating the reservoir domain. The reservoir domain is defined based on the microseismic events cloud recorded during the well stimulation. This microseismic cloud represents stimulated reservoir volume (SRV) which represents the rock volume where hydraulic fractures propagated, or natural fractures were activated by pressure-stress perturbations during stimulation. Figure A - 2 illustrates the microseismic events at the Red site, with events color-coded to distinguish those observed during injector stimulation (blue dots) from those during producer stimulation (red dots). To quantitatively define the SRV boundaries, a histogram of high-quality events was generated using 100 ft bins. The SRV boundary was established by selecting bins containing more than 100 events from either stimulation treatment. This microseismic-based methodology yielded an SRV with a length of 2,300 ft and a height of 2,500 ft. The reservoir domain is defined to encompass this SRV.

Based on the estimated SRV, the reservoir domain is defined as shown in Figure A - 3. The reservoir domain extends 3300 ft×5250 ft×3000 ft. This reservoir domain is discretized into uniform grid blocks of 30 ft×15 ft×300 ft, resulting in 110×350×10 (385,000 cells in total). The top layer depth is 6500 ft. The injector and producer are around 360 ft apart horizontally and 300 ft apart in vertical. The cluster spacing is set to 30 ft, with a single hydraulic fracture assumed to initiate and propagate from each perforation cluster. It is noted that the injector contains a greater number of perforation clusters, corresponding to a longer lateral section.

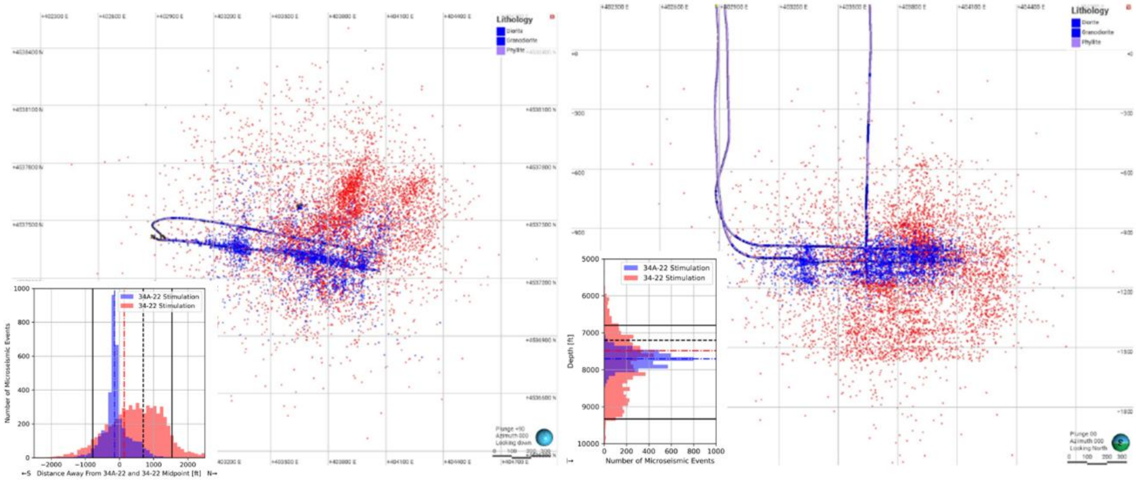

Figure A - 2: Microseismic event clouds and their histogram (Norbeck & Latimer, 2023)

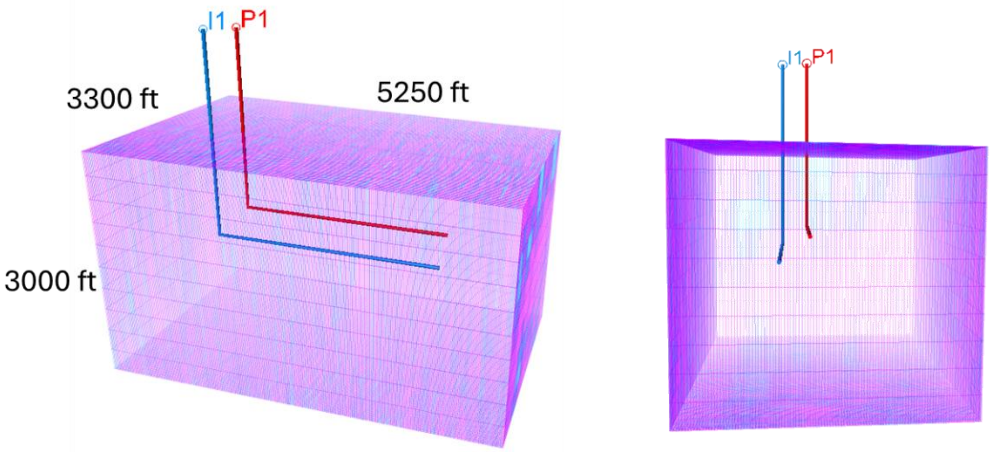

Figure A - 3: Well trajectory and reservoir domain

Subsequently, a geological model was developed assuming a typical tight reservoir characterized by numerous in-situ natural fractures. The natural fractures are generally aligned with the orientation of the hydraulic fractures, though slight deviations occur due to variations in the in-situ stress field over geological time. To capture this anisotropic behavior, a variogram with a longer correlation range in the major direction was assigned. Using Gaussian random simulation, the porosity distribution was generated, as illustrated in Figure A - 4. The mean is 0.01 and std is 0.001, range of major direction is 500 ft and minor direction is 10 ft. Then, the permeability realization was created using co-kriging with porosity. The mean is 10^{-4} md and std is 10^{-5} md. Vertical permeability is defined as 0.1 of horizontal permeability (kv/kh = 0.1) and the model has isotropic horizontal permeability.

Next, the SRV and hydraulic fractures were modeled based on the generated porosity and permeability realizations. The SRV is characterized by enhanced porosity and permeability resulting from the activation of natural fractures. This effect was represented by applying a multiplier of 10 to both properties within the SRV region. Hydraulic fractures were then modeled assuming vertical and horizontal symmetry for both the injector and producer wells. Each fracture has a half-length of 810 ft and a half-height of 450 ft. The resulting geological realization is visualized in Figure A - 5.

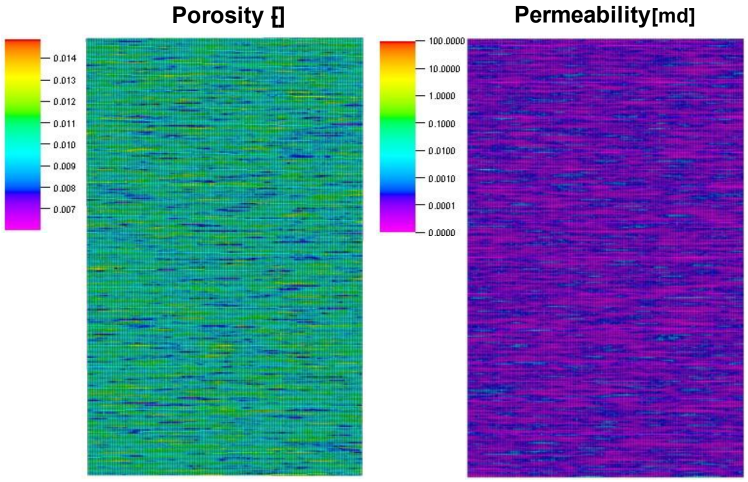

Figure A - 4: Porosity and permeability distribution

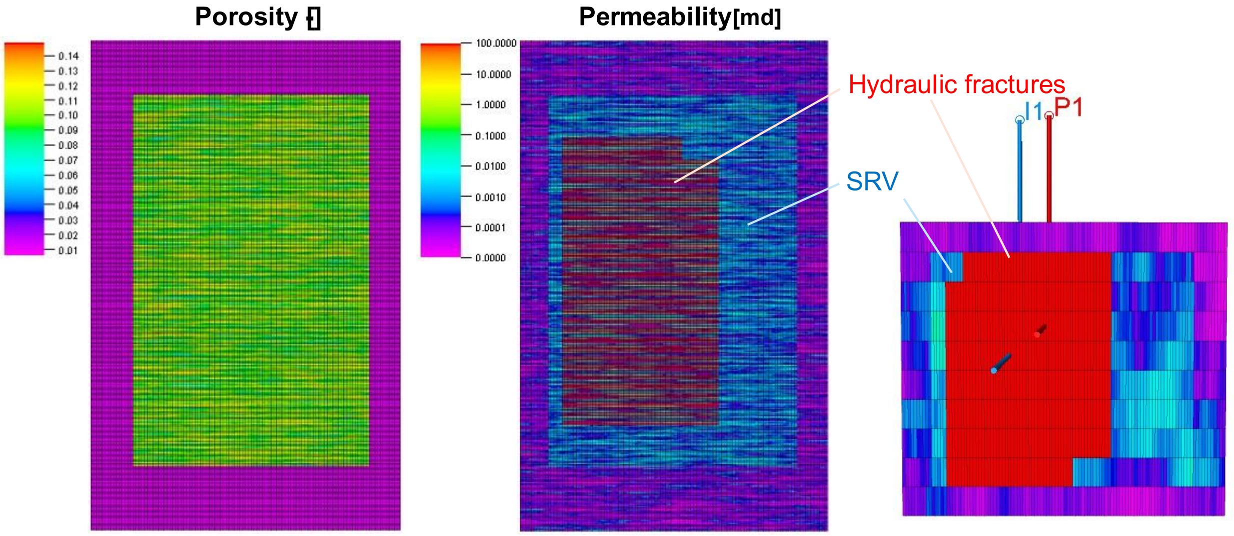

Figure A - 5: Porosity and permeability distribution with SRV and hydraulic fractures

Eclipse Compositional Simulator with Thermal option is utilized to create reservoir simulation deck. The key fluid and thermal properties are consistent with those reported in Chan et al. (2026). To represent the Dirichlet boundary condition, large pore volume and rock volume multipliers ($\times 10^4$) were assigned to the boundary cells. The initial pressure distribution was defined assuming a normal pressure gradient of 0.44 psi/ft, while the geothermal gradient was determined based on the temperature reading from Figure A - 1. The resulting initial pressure and temperature distributions are presented in Figure A - 6.

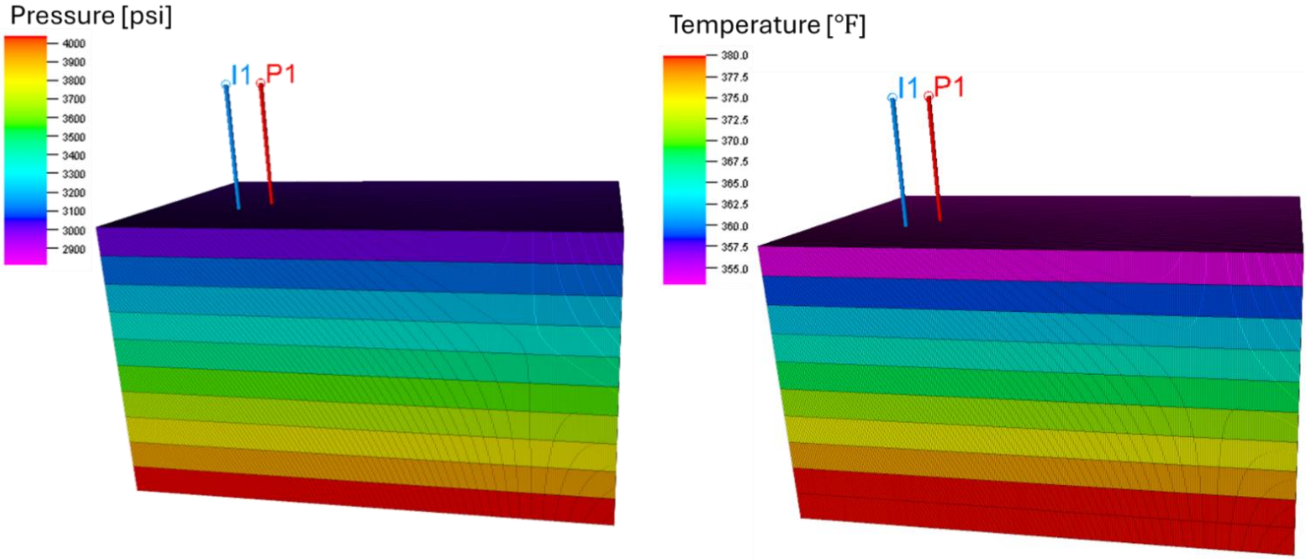

Figure A - 6: Initial pressure and temperature

Reservoir simulations were conducted using the established model. The injection well was controlled by a constant rate of 63 L/s (34,236 bbl/d), while the production well was maintained at a constant bottomhole pressure (BHP) of 3,000 psi. The bottomhole injection temperature was specified as 105 °F. This temperature, slightly elevated from surface conditions, accounts for conductive heat gain within the wellbore, as observed in Utah FORGE application (Smith et al., 2025).

The simulated well thermal performance is presented in Figure A-7. The model predicts a stable production plateau (temperature and energy) for approximately two years, after which thermal decline initiates. This finding is consistent with field observations by Norbeck et al. (2024), who reported no evident thermal degradation during the project's initial 6,200 hours of operation. The developed model's initial production temperature of 365°F is reasonably aligned with the 341°F reported from the field (Norbeck et al., 2024). The 24 °F difference is attributed to the model predicting bottomhole temperature, while the field measurement reflects surface temperature after conductive heat losses in the wellbore, an effect documented at the Utah FORGE site (Smith et al., 2025). In terms of energy production, the model's stable output of 45 MWth during the stable production period compares favorably with the 3.5 MWe electrical capacity demonstrated by field flow tests (Norbeck & Latimer, 2023). Applying a standard Organic Rankine Cycle (ORC) conversion factor of 8%

(0.08) to the model's thermal output yields an estimated electrical production of 3.6 MWe, showing strong agreement with the reported field potential.

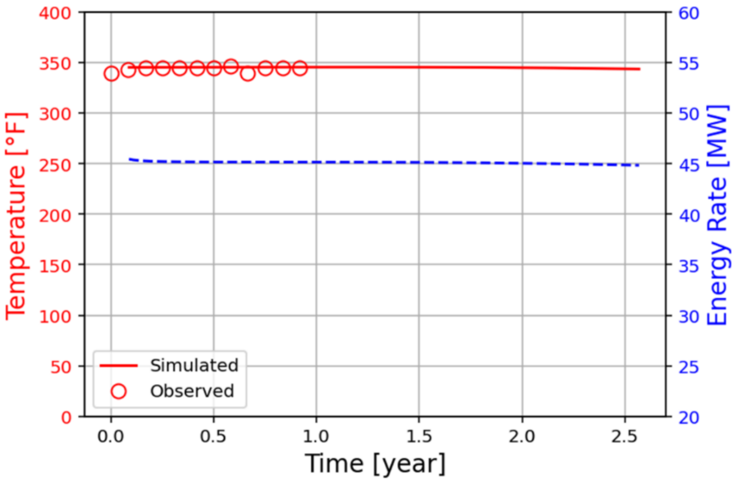

Figure A - 7: Well thermal performance of synthetic Red model